On the characterization of charge-transfer effects in non-covalently bound molecular complexes

Yuezhi Mao,[†] Qinghui Ge,[†,‡] Paul R. Horn,[†] and Martin Head-Gordon[*,†,‡]

† *Kenneth S. Pitzer Center for Theoretical Chemistry, Department of Chemistry, University of California at Berkeley, Berkeley, CA 94720, USA*

‡ *Chemical Sciences Division, Lawrence Berkeley National Laboratory, Berkeley, CA 94720, USA*

E-mail: mhg@cchem.berkeley.edu

Abstract

Charge-transfer (CT) is an important binding force in the formation of intermolecular complexes, and there have been a variety of theoretical models proposed to quantify this effect. These approaches, which typically rely on a definition of a "CT-free" state based on a partition of the system, sometimes yield significantly different results for a given intermolecular complex. Two widely used definitions of the "CT-free" state, the absolutely localized molecular orbitals (ALMO) method (where only on-fragment orbital mixings are permitted) and the constrained density functional theory (CDFT) approach (where fragment electron populations are fixed), are carefully examined in this work. Natural bond orbital (NBO) and the regularized symmetry-adapted perturbation theory (SAPT) are also briefly considered. Results for the ALMO and CDFT definitions of CT are compared on a broad range of model systems, including hydrogen-bonding systems, borane complexes, metal-carbonyl complexes, and complexes formed

by water and metal cations. For most of these systems, CDFT yields a much smaller equilibrium CT energy compared to that given by the ALMO-based definition. This is mainly because the CDFT population constraint does not fully inhibit CT, which means that the CDFT "CT-free" state is in fact CT-contaminated. Examples of this contamination include (i) matching forward and backward donation (e.g. formic acid dimer), and (ii) unidirectional CT without changing fragment populations. The magnitude of the latter effect is quantified in systems such as the water dimer by employing a 3-space density constraint in addition to the orbital constraint. Furthermore, by means of the adiabatic EDA, it is shown that several observable effects of CT, such as the "pyramidalization" of the planar BH_3 molecule upon the complexation with Lewis bases, already appear on the "CT-free" CDFT surface. These results reveal the essential distinctions between the ALMO and CDFT definitions of CT, and suggest that the former is more consistent with accepted understanding of the role of CT in intermolecular binding.

1 Introduction

The charge-transfer (CT) phenomenon, in the context of intermolecular interaction, usually refers to the stabilization effect arising from the intermolecular relaxation of the system wavefunction. As indicated by its name, CT is often accompanied with changes in the charge populations of the binding moieties. Given a complex consisting of an electron donor (D) and acceptor (A), CT can also be viewed as a partial mixing of the higher-energy ionic state $|D^+A^-\rangle$ into the neutral state $|DA\rangle$, which thus lowers the ground state energy of the system.[1] Note that CT discussed in this paper is a phenomenon accompanied with formation of ground state complexes, which is essentially a delocalization effect due to the quantum nature of electrons, and it differs from other widely studied concepts such as electron-transfer (ET) reactions[2,3] where integral number of electron(s) is/are transfered. Therefore, the term

"charge delocalization", instead of "charge transfer", was suggested by Misquitta[4] to refer to this phenomenon.

As an important binding force besides electrostatic interaction and dispersion, the effect of CT is ubiquitous in non-covalently bound complexes. For systems where the CT effect is non-trivial, the magnitude of the associated stabilization energy ranges from a few kJ/mol in simple hydrogen-bonding complexes, to hundreds of kJ/mol in strong dative compounds. CT also plays an important role in radical chemistry, since an open-shell species can serve as either electron donor or acceptor.[5–8] Beyond energetic effects, CT reveals itself via abundant observable consequences, such as changes in structural and vibrational properties of the binding moieties. For instance, the elongation of the X–H bond and the red shift in the X–H stretch frequency upon the formation of the X–H$\cdots$Y hydrogen bond are widely believed to be consequences of CT[9–15] (although alternative interpretations also exist[16–18]). Nonetheless, the CT energy itself is not an observable in quantum mechanics, so it is almost impossible to measure the stabilization and other effects directly in experiment, although a series of molecular beam scattering experiments that extract the CT component indirectly based on several assumptions have been reported.[19–21]

Theoretical models of CT, on the other hand, are valuable tools for characterizing this important effect in intermolecular binding. They also facilitate the efforts to incorporate the CT component explicitly in advanced molecular force fields.[22–26] Most of these models are associated with energy decomposition analysis (EDA)[27] schemes, and they often rely on the preparation of a "CT-free" reference state, on which CT between molecules is forbidden subject to a certain criterion. The CT energy is then evaluated with a subtraction ($\Delta E_{\mathrm{CT}} = E_{\mathrm{full}} - E_{\mathrm{CT\text{-}free}}$) or using perturbation theory. Therefore, the characteristics of a given CT model are implicitly determined by its definition of this intermediate state.

The natural bonding orbital (NBO) method[28,29] constructs a set of mutually orthogonal occupied orbitals (the "Lewis" orbitals, including core, lone-pair and bonding orbitals)

from a density matrix derived from a fully converged self-consistent field (SCF) calculation, whereby the reference state is defined. The CT stabilization energy is then defined as the interaction between donor's bonding/lone-pair orbitals and acceptor's anti-bonding orbitals via the Fock operator, which can be calculated by deleting the corresponding off-diagonal blocks in the Fock matrix (see Ref. 28 for details). Another closely related approach is the natural energy decomposition analysis (NEDA) scheme,[30–32] where the CT term is defined as the difference between the energy of the fully relaxed supersystem wavefunction and that of the state constructed from the "Lewis" orbitals. These approaches are often found to generate excessively large CT energies, and a recent investigation by Stone[33] has shown that the globally orthogonalized "Lewis" orbitals obtained from the NBO procedure, which are *not* variationally optimized, provide a rather poor description for the electronic structure of the supersystem energetically. This high-energy reference state, as pointed out by Stone, is likely to be responsible for the overly large CT values given by NBO.[33,34]

Symmetry-adapted perturbation theory (SAPT),[35,36] by its original formulation, does not separate out CT as an individual term. The intra- and intermolecular orbital relaxation due to the presence of other molecules, i.e., polarization (POL) and CT, both belong to the induction term in SAPT. Several methods have been proposed to extract CT energy from the induction energy of SAPT. It was first suggested that the CT energy can be evaluated as the difference in second-order induction (and exchange-induction) energy calculated with dimer-centered (supersystem) basis and monomer-centered basis.[37,38] However, it is evident that CT under this definition vanishes when monomer basis becomes complete. To overcome the drawbacks of this approach, Misquitta proposed an alternative method[4] under the framework of SAPT(DFT),[39] which employs a regularized (damped in the short range) Coulomb potential for fragment B's nuclei to suppress the $A \to B$ charge transfer. The CT

energy at the second-order of SAPT is then defined as

$$E_{\mathrm{CT}}^{(2)} = [E_{\mathrm{ind}}^{(2)} - E_{\mathrm{ind}}^{(2)}(\mathrm{Reg})] + [E_{\mathrm{ind\text{-}exch}}^{(2)} - E_{\mathrm{ind\text{-}exch}}^{(2)}(\mathrm{Reg})] \tag{1}$$

Note that the total second-order CT energy is the sum of the $A \to B$ and $B \to A$ contributions. This method will be further discussed in Sec. 3.7.

In contrast to the NBO and SAPT-based methods, many other EDA schemes originating from the Kitaura-Morokuma (KM)-EDA[40,41] access the "CT-free" state via a variational optimization. It is most straightforward to separate POL and CT through a partition in the orbital space, i.e., given fragments A and B, the mixing of A's virtual orbitals (V_A) into its own occupied orbitals (O_A) in the presence of B is defined as the polarization of A, while the rotation of O_A into $V_A \oplus V_B$ with O_B remaining frozen further incorporates the $A \to B$ CT. This is exactly how early EDA approaches such as the reduced variational space (RVS)[42] and the similar constrained space orbital variation (CSOV)[43] methods are formulated. However, as distinct "CT-free" states are employed to obtain the $A \to B$ and $B \to A$ contributions, the CT (and POL) terms computed thereby do not add up to the full variational energy lowering, and thus higher-order relaxation effect is not incorporated.

The later proposed absolutely localized molecular orbital (ALMO)-EDA[44–46] (and the closely related block-localized wavefunction (BLW)[47–49] method) overcomes this problem, by employing a single "CT-free" state for the entire system. Starting from the supersystem wavefunction constructed with isolated fragment molecular orbitals (MOs), i.e., the frozen state (Ψ_{frz}), the polarized yet "CT-free" intermediate state is obtained through a variational optimization subject to the constraint that the MOs on each fragment are only expanded by in its own atomic orbital (AO) basis functions, i.e., the AO-to-MO coefficient matrix has a fragment-block-diagonal structure. The energy lowering relative to the frozen state is

defined as the polarization energy (ΔE_{pol}):

$$\Delta E_{\mathrm{pol}} = E[\Psi_{\mathrm{ALMO}}] - E[\Psi_{\mathrm{frz}}] \tag{2}$$

The CT energy is then defined as the energy lowering due to the further relaxation of the system wavefunction upon the removal of the ALMO constraint:

$$\Delta E_{\mathrm{CT}} = E[\Psi_{\mathrm{full}}] - E[\Psi_{\mathrm{ALMO}}] \tag{3}$$

Note that the basis set superposition error (BSSE) can be removed from the right-hand side (RHS) of Eq. (3) if desired, by applying a counterpoise correction.[50] An ALMO-based charge-transfer analysis (CTA) that utilizes the same "CT-free" state has also been proposed,[51] which is able to decompose the transfered electron density (ΔQ), as well as the associated ΔE_{CT}, into pairwise forward and backward contributions. The ALMO-EDA and CTA have been successfully applied to quantifying CT in small water clusters,[52] naphthalene-benzene radical cation complexes,[7] ionized glycerol complex,[53] etc. More details about this method, including recent development to achieve a meaningful basis set limit for the POL and CT components, are introduced in Sec. 2.1.

The density-based EDA (DEDA),[54] on the other hand, relies on a population-based definition of CT: the "CT-free" state is prepared by performing a constrained density functional theory (CDFT)[55–57] calculation that variationally optimizes the supersystem wavefunction while conserving charge population of each fragment to a preset value. Real-space partitioning methods, such as the Becke[58] and Hirshfeld[59] schemes, are found to be compatible with the CDFT approach. While we refer the reader to Sec. 2 for more details, we note that several desirable features of the CDFT definition have been shown/argued recently: (i) the resulting CT energy (ΔE_{CT}) is stable with respect to basis set, and by construction it is BSSE-free;[60,61] (ii) E_{CT} evaluated with CDFT shows better linear correlation with the amount of transferred

charge (Δq) and the reciprocal of the IP(donor)-EA(acceptor) gap compared to other methods[61] (IP: ionization potential; EA: electron affinity). It has also been noticed that CDFT usually yields smaller CT energies than ALMO or BLW approaches,[61] and the role of CT is thus less emphasized in the resulting energy decomposition.[62]

The lack of a unique definition of CT in theoretical models has made it "*the source of a good deal of error and confusion*" (Stone).[1] For the water dimer, a prototypical system for intermolecular hydrogen bonding, the magnitude of CT stabilization energy produced by different methods varies significantly (collected in Table 1; also see Table 1 in Ref. 63), leading to inconsistent interpretations of the nature of this hydrogen bond. While the NBO analysis clearly suggests that CT is predominant since the water dimer is unbound without CT at its equilibrium geometry, the ALMO-EDA and other variational methods based on orbital-space partitions suggest no more significant role of CT than other components such as frozen interaction (FRZ) and POL, and even smaller CT energies are given by the CDFT and regularized SAPT methods.

The goal of the present paper is to at least partly resolve the confusions caused by distinct definitions of CT. With a broad range of simple model systems, we elucidate the essential differences between definitions based on orbital-space partitions and those based on population changes, using ALMO and CDFT as respective representatives. Moreover, the recently proposed "adiabatic EDA" approach[68] is utilized to demonstrate the differences in calculated observable consequences of CT subject to these two definitions, which aims to assess their capability of characterizing well-established phenomena of CT in chemistry. Other related aspects, such as the differences between the results of ALMO and regularized SAPT, are also discussed in this paper.

Table 1: CT stabilization energy (in kJ/mol) for the equilibrium water dimer reported in literature, showing differences that are much larger than can be associated with different choices of electronic structure method, and different optimized water dimer geometries.

Method	CT energy	Reference
NBO	-38.37	64
NEDA	-37.28	32
KM-EDA	-8.83	40
	-5.19	65 [a]
RVS	-3.56	42
ALMO-EDA (I)	-7.3	66
ALMO-EDA (II) [b]	-7.74	46
CDFT(Becke)	-2.8	54
CDFT(FBH) [c]	-3.31	60
IMPT [d]	-3.49	37
SM09 [e]	-2.65	38
Regularized SAPT	-1.49	4

[a] The method in Ref. 65 is essentially the KM scheme with BSSE corrected.

[b] (I)/(II) refers to the first-/second-generation ALMO-EDA.

[c] The definition of "Becke" and "FBH" can be found in Sec. 2.2.

[d] IMPT stands for intermolecular perturbation theory.[67]

[e] "SM09" stands for the method reported in Ref. 38 under the framework of SAPT(DFT).

2 Methods

2.1 ALMO-based definition of CT

The ALMO approach defines the "CT-free" state through a partition in the orbital space. It first constructs the frozen wavefunction of the complex by concatenating the fragment wavefunctions optimized in isolation with full antisymmetrization. The associated one-particle density matrix (1PDM), $\mathbf{P}_{\text{frz}}$, can be represented as

$$\mathbf{P}_{\text{frz}} = (\mathbf{C}_o)_{\text{frz}}(\boldsymbol{\sigma}_{\text{frz}}^{-1})(\mathbf{C}_o)_{\text{frz}}^T, \tag{4}$$

where $(\mathbf{C}_o)_{\text{frz}}$ is an AO-to-MO coefficient matrix containing occupied fragment MOs on its diagonal blocks (as illustrated in Fig. 1), and $\boldsymbol{\sigma}_{\text{frz}}$ is the overlap between these orbitals ($\mathbf{S}$ is the AO overlap matrix):

$$\boldsymbol{\sigma}_{\text{frz}} = (\mathbf{C}_o)_{\text{frz}}^T\mathbf{S}(\mathbf{C}_o)_{\text{frz}}. \tag{5}$$

With the 1PDM defined as in Eq. (4), the energy functional $E[\mathbf{P}]$ is then minimized while maintaining the fragment-block-diagonal structure of the MO coefficient matrix, i.e., the MOs are "absolutely localized" on each fragment. Such a variational optimization, which is called "SCF for molecular interaction" (SCF-MI)[69] for historical reasons, can be performed by solving locally projected SCF equations[69–71] (we refer the reader to Ref. 71 for more technical details) or by gradient-based algorithms. The resulting ALMOs, as shown in Fig. 1, are thus polarized in a fully self-consistent fashion within a properly antisymmetrized wavefunction. Such on-fragment orbital relaxations, on the other hand, do not give rise to charge flow between fragments under the Mulliken definition. Therefore, the "CT-free" state is fully defined by these polarized ALMOs, and the CT energy can be obtained by further computing its energy difference against the unconstrained SCF solution (Eq. (3)).

As for many other CT models based on orbital-space partitioning, the original ALMO

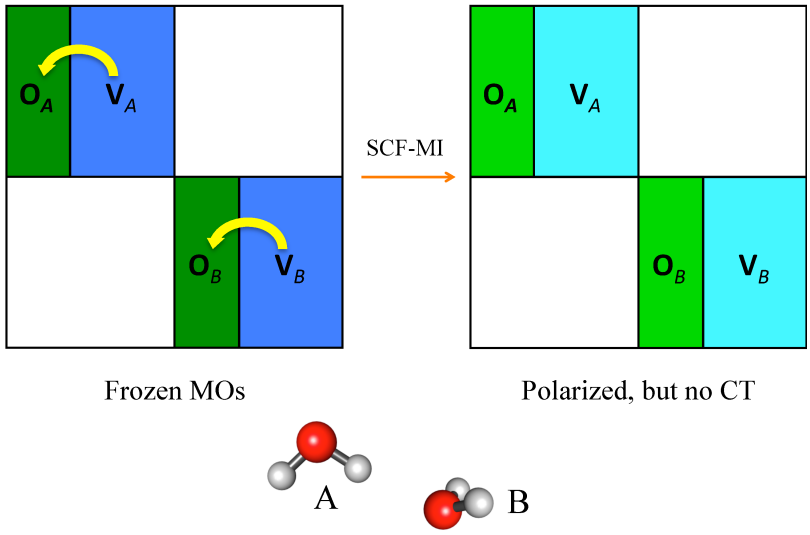

Figure 1: Illustration of the ALMO definition of the polarized yet "CT-free" state for the water dimer, obtained by performing a variational optimization (SCF-MI) from the frozen wavefunction. O and V stand for the occupied and virtual MOs on each fragment.

definition of CT energy lacks a well-defined basis set limit.[61,72] This is because when the size of the employed basis set grows, an AO basis function assigned to a certain fragment can easily overlap those on other fragments in 3-space such that the boundary between intra- and interfragment relaxations becomes ambiguous. To address this shortcoming, a new approach was proposed by some of us[73] to construct the polarization subspace of each fragment using their fragment electrical response functions (FERFs), whose basic spirit is to truncate the virtual space of each fragment so that degrees of freedom irrelevant to responses to external electric fields (polarization) are excluded in the SCF-MI calculation. The orbital response of a fragment to an external electric field can be captured by solving a set of coupled-perturbed (CP)SCF equations:

$$H_{ai,bj}(\Delta_\mu)_{bj} = (M_\mu)_{ai}, \tag{6}$$

where $\mathbf{H}$ is the SCF orbital Hessian and $\mathbf{M}_\mu$ is one component of the multipole matrix at a certain order, i, j and a, b are indices for occupied and virtual fragment MOs, respectively. The truncation of the original virtual space (spanned by $\mathbf{C}_v$) is achieved by performing a

singular value decomposition (SVD) for each Δ_μ:

$$(\Delta_\mu)_{bj} = (L_\mu)_{ba}(d_\mu)_{ai}(R_\mu)_{ij} \tag{7}$$

$$\mathbf{V}_\mu = \mathbf{C}_v\tilde{\mathbf{L}}_\mu \tag{8}$$

where $\tilde{\mathbf{L}}_\mu$ refers to the first n_{occ} vectors of $\mathbf{L}_\mu$ (i.e. only n_{occ} virtual orbitals determine the exact linear response to $\mathbf{M}_\mu$).

Numerical results presented in Ref. 73 show that including both the three dipole- (D) and five quadrupole-type (Q) response functions per occupied orbital is sufficient to correctly reproduce the asymptotic behavior of electrical polarization, as well as providing a well-behaved basis set limit. The corresponding polarization subspace of a given fragment A is

$$\begin{aligned}\text{Pol}_A = \mathbf{O}_A \oplus \text{span}\{\mathbf{V}_{Dx}, \mathbf{V}_{Dy}, \mathbf{V}_{Dz}\}\oplus \\ \text{span}\{\mathbf{V}_{Q2,-2}, \mathbf{V}_{Q2,-1}, \mathbf{V}_{Q2,0}, \mathbf{V}_{Q2,1}, \mathbf{V}_{Q2,2}\}\end{aligned} \tag{9}$$

This model, with $8n_{\text{occ}}$ virtual FERFs, is denoted as "FERF-nDQ" ("n" means that the MOs are *nonorthogonal* across fragments) and is employed in all FERF-related calculations in this paper.

2.2 CDFT-based definition of CT

The details of CDFT calculations have been documented in the previous papers by Wu and Van Voorhis,[55,56] and here we briefly recapitulate the basics. The energy functional to be optimized can be represented as

$$E[\rho] = E_0[\rho] + \sum_c \lambda_c \left(\int \rho(\mathbf{r}) w_c(\mathbf{r}) \mathrm{d}\mathbf{r} - N_c \right) \tag{10}$$

where $E_0[\rho]$ is the standard Kohn-Sham (KS) energy functional. For each constraint in Eq. (10), $w_c(\mathbf{r})$ is the weighting function that corresponds to the constrained property, N_c is the value to be imposed in the calculation, and λ_c is the Lagrangian multiplier. The associated Fock matrix also contains an additional constraining potential:

$$\mathbf{F} = \mathbf{F}_0 + \sum_c \lambda_c \mathbf{W}_c, \tag{11}$$

where $\mathbf{F}_0 = \partial E_0 / \partial \mathbf{P}$, and $\mathbf{W}_c$ is the weighting function represented in the AO basis:

$$(W_c)_{\mu\nu} = \int w_c(\mathbf{r}) \chi_\mu(\mathbf{r}) \chi_\nu(\mathbf{r}) \mathrm{d}\mathbf{r} \tag{12}$$

The energy functional given by Eq. (10) can thus be optimized through a double-loop SCF approach. While the outer loop updates $\mathbf{F}_0$, the inner loop searches for a set of Lagrangian multipliers to ensure that the density from diagonalizing $\mathbf{F}$ satisfies the constraints, using the first and second derivatives of E with respect to λ_c's whose forms have been previously derived.[55,56]

CDFT has been successfully applied to the study of ET reactions that involve integer-number electron transfer from donor to acceptor,[74–77] while its application to modeling CT in the context of intermolecular interaction appeared more recently. The latter category of problems is more challenging for CDFT, because the result can be sensitive to the choice of partitioning schemes and the means used to generate constrained values (initial fragment charge populations). The DEDA by Wu et al.[54] employs the Becke partitioning scheme[58] (using "fuzzy", shifted Voronoi cells): for each fragment, zero weights are assigned to grid points out of its corresponding Becke cell, and the fragment weight matrix can thus be calculated using Eq. (12). The initial population of each fragment is determined by projecting the promolecule density (sum of isolated fragment densities) onto the corresponding weighting function. Using $\rho_0(\mathbf{r})$ to represent the promolecule density, the energy functional can be

rewritten as

$$E[\rho] = E_0[\rho] + \sum_A \lambda_A \int (\rho(\mathbf{r}) - \rho_0(\mathbf{r}))\, w_A(\mathbf{r}) \mathrm{d}\mathbf{r} \tag{13}$$

where the sum is over fragments whose populations are constrained.

The above-mentioned approach (which is denoted as "CDFT(Becke)" in this paper) was recently revisited by others[61,62] and was found to yield reasonable CT stabilization energies. We should bear in mind that with this approach, the number of electrons to be constrained on each fragment ($N_A = \int \rho_0(\mathbf{r}) w_A(\mathbf{r}) \mathrm{d}\mathbf{r}$) is usually *not* an integer, which might be unnatural to think about. The option to impose integer fragment charges has also been investigated by Řezáč and de la Lande with various population schemes,[60] and it was demonstrated that a fragment-based Hirshfeld (FBH) partition can yield reasonable results while conserving integer fragment charge populations. The corresponding weighting functions are evaluated using isolated fragment densities ($\rho_A(\mathbf{r})$):

$$w_A^{\mathrm{FBH}}(\mathbf{r}) = \frac{\rho_A(\mathbf{r})}{\sum_A \rho_A(\mathbf{r})} = \rho_A(\mathbf{r})/\rho_0(\mathbf{r}) \tag{14}$$

It should be noted that the "Becke" scheme investigated in Ref. 60 also imposes integer charge population on each fragment so it behaves in a completely different way than the CDFT(Becke) approach introduced above.

In this work, we investigate both the Becke and FBH population schemes for CDFT calculations of CT. These real-space partitions ensure that the *net charge flow* between fragments is zero in the 3-space, which is illustrated in Fig. 2.

2.3 Characterization of constant-density CT

The frozen state in Wu's DEDA[54] is determined by optimizing the supersystem wavefunction subject to the constraint that the 3-space density is unchanged relative to the promolecule density, using a constrained search algorithm.[78] This constraint is much stronger than con-

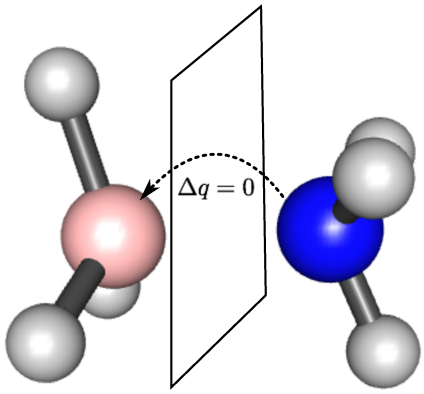

Figure 2: Illustration of the CDFT definition of the "CT-free" state. The plane stands for a partition of the 3-space, across which the net charge flow is constrained to be zero. In practice, this is accomplished by enforcing constant values of the total fragment charge, by measures such as the Becke and fragment-based Hirshfeld (FBH) definitions.

serving fragment charge populations so the resulting variational energy is guaranteed to be an upper bound to that given by optimizing Eq. (13).

In order to characterize this constant-density relaxation effect, Horn and Head-Gordon proposed an alternative approach[79] employing a penalty function for the difference in 3-space density, where the metric of the error is chosen to be the Coulomb repulsion of the difference density with itself. The energy functional can be written as

$$E[\mathbf{P}] = E_0[\mathbf{P}] + \lambda \int \mathrm{d}\mathbf{r}_1 \mathrm{d}\mathbf{r}_2 \Delta\rho(\mathbf{r}_1) \frac{1}{r_{12}} \Delta\rho(\mathbf{r}_2) \tag{15}$$

where $\Delta\rho(\mathbf{r}) = \rho(\mathbf{r}) - \rho_{\mathrm{target}}(\mathbf{r})$, and λ is a scaling parameter that controls the magnitude of the penalty, which can be monotonically increased to impose the constraint as strictly as possible. It has been shown in Ref. 79 that when the target density is set to be the sum of isolated fragment densities, this approach is able to reproduce the energy lowering associated with the constant density relaxation in DEDA when λ is moderately large (note that both methods are unable to impose the density constraint exactly). In this paper, however, we use the density associated with the properly antisymmetrized frozen wavefunction (ρ_{frz}) as

the target density exclusively.

With a given λ, either SCF-MI (enabling on-fragment relaxations only) or full SCF calculations could be performed to minimize the energy functional given by Eq. (15). The energy lowering associated with the former is defined as the constant-density (const-ρ) polarization, while the energy difference between the two corresponds to the const-ρ CT. Subject to a population scheme based on real-space partitioning, const-ρ CT occurs without changing fragment populations so it is not characterized as CT by CDFT-based models. Therefore, the evaluation of this quantity can provide useful insights into the numerical difference between ALMO and CDFT definitions, as illustrated in Sec. 3.

2.4 Characterization of the observable effects of CT

The methods introduced above are concerned with the evaluation of CT energy at a single geometry. In order to characterize the observable consequences of the components of intermolecular interactions, a reformulation of the ALMO-EDA in an adiabatic picture was recently reported by some of us.[68] In this scheme, the geometry of the intermolecular complex is relaxed on the potential energy surface (PES) of each intermediate state (frozen, polarized, and fully relaxed) following the associated analytical gradients until a stationary point is reached. Molecular properties other than geometry, such as vibrational frequencies, multipole moments, can also be evaluated at these stationary points. By comparing the properties calculated on the "CT-free" state and those on the fully relaxed state, the effect of CT on these observables can be exhibited. Such calculations have also been reported by others using the (original) ALMO-EDA[13,68] and the BLW-EDA[49,80–82] , as they share the same definition for the "CT-free" state whose analytical nuclear gradient is easy to obtain.[83]

The equations required to perform an adiabatic ALMO-EDA are available in Ref. 68. In this work, we extend the concept of "adiabatic EDA" to the CDFT definition of CT, and the observable consequences of CT thus computed can be compared against those obtained

by using the ALMO definition. The equations for the nuclear gradient of CDFT with the Becke partitioning scheme are presented in Appendix A.

3 Results

3.1 Computational details

The calculations in this work are performed with a development version of the Q-Chem 4.4 software package,[84] where the energy calculation using CDFT(FBH) and the nuclear gradient of the CDFT(Becke) approach were implemented for this work. Unless otherwise specified, the ωB97X-V[85] functional, which is a range-separated hybrid GGA with the VV10[86] dispersion correction, is employed for the calculations. Based on extensive benchmarking[87–89] and our experience from previous EDA studies,[68,90,91] this functional is amongst the most accurate available for intermolecular interactions. A fairly dense (75, 302) grid (75 radial shells for each atom with 302 Lebedev points in each) is employed for the integration of the exchange-correlation (XC) functional, while a smaller SG-1 grid[92] is used for the VV10 nonlocal correlation functional. The employed basis sets are specified with the results presented below. All the SCF calculations are converged to 10^{-8} a.u., and the geometry optimizations are converged when the maximum component of the nuclear gradient is below 10^{-4} a.u..

Unless otherwise noted, the CT stabilization energies based on the ALMO definition are evaluated with the aforementioned FERF-nDQ model, while the original ALMO approach based on AO-blocking is used for adiabatic EDA calculations, as the analytical gradient of SCF-MI using FERFs is not available yet. For the constant-density optimizations (see Sec. 2.3), the penalty parameter λ is chosen to be 2.0×10^3 as suggested in Ref. 79, and the FERF-nDQ model is employed to further separate the const-ρ energy lowering into POL and CT contributions.

3.2 Cyclic H-bonding system

The difference between the ALMO and CDFT definition of CT can be most clearly revealed via a cyclic, double hydrogen-bonded system, such as the formic acid dimer (Fig. 3), as well as the *p*-biphthalate dimer (a so-called "anti-electrostatic H-bonding" (AEHB) complex) studied by us in a previous paper,[46] and the pyridine dimer (C_{2h}) studied in Ref. 4. To simplify the discussion, below we focus on the formic acid dimer.

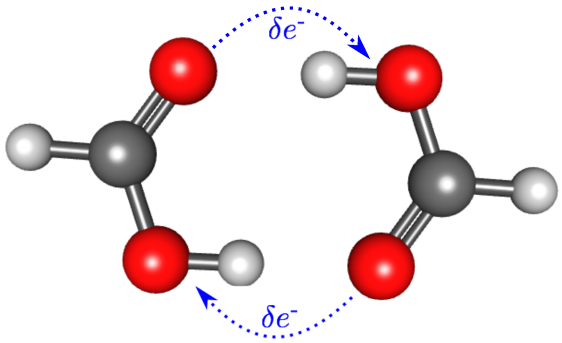

Figure 3: Geometry of the formic acid dimer (of C_{2h} symmetry). The arrows indicate that the net charge flow between two formic acid molecules is zero, even though CT will occur between the monomers in each of the two identical hydrogen bonds.

The equilibrium POL and CT energies, as well as the POL- and CT-induced changes in the relevant observables calculated by AO-based ALMO, FERF-nDQ, and CDFT are presented in Table 2 (the original data for the observable calculations are available in Table S1 of the Supporting Information). The most noticeable feature is that the energy contribution from CT is zero with the CDFT definition, and therefore so is the effect of CT on the observables. This can be easily understood through the formalism of the CDFT approach: due to the symmetry of this system, the forward and backward donations across the molecular boundary (under a given definition) exactly cancel each other in terms of the resulting population change, which thus automatically satisfies the constraint on fragment populations. As a result, the "CT-free" state is identical to the fully relaxed state under the CDFT

definition, and the stabilization energy and the shifts in observables beyond the frozen level are entirely characterized as effects of polarization.

Table 2: Equilibrium POL and CT energies (in kJ/mol) and observable shifts induced by POL and CT for the formic acid dimer calculated with three distinct models. The observable shifts due to POL are measured against the values obtained on the common frozen state, and the shifts due to CT are relative to the values obtained on the "CT-free" state of each model. Δr_{OH} and $\Delta r_{\mathrm{O\cdot\cdot H}}$ (in Å) refer to the changes in the lengths of the proton-donating O–H bond and the hydrogen bond (O··H distance), respectively. $\Delta\angle_{\mathrm{OH\cdot\cdot O}}$ (°) stands for the increase in the hydrogen-bond angle, and $\Delta\nu_{\mathrm{OH}}$ for the red shift in the OH stretch frequency (in cm^{-1}). All the calculations are performed at the ωB97X-V/def2-TZVPPD level of theory.

	Effects of POL			Effects of CT		
	ALMO	FERF	CDFT	ALMO	FERF	CDFT
ΔE	-44.90	-41.87	-90.82	-45.92	-48.94	0
Δr_{OH}	0.004	0.003	0.028	0.024	0.025	0
$\Delta r_{\mathrm{O\cdot\cdot H}}$	-0.20	-0.18	-0.53	-0.33	-0.35	0
$\Delta\angle_{\mathrm{OH\cdot\cdot O}}$	0.26	0.24	5.52	5.26	5.28	0
$\Delta\nu_{\mathrm{OH}}$	70	61	538	468	478	0

The ALMO-based methods, on the other hand, suggest a significant contribution from CT for this system. CT accounts for roughly 50% of the equilibrium interaction energy (-82.27 kJ/mol), which is a usually larger proportion than in other typical neutral H-bonding complexes (see Sec. 3.3). The calculated CT-induced changes in the proton-donating O–H bond, such as its elongation and the red shift in its stretch frequency, are also remarkable. In contrast, POL has a much smaller effect on these observables, although it stabilizes the system roughly as much as CT at the equilibrium geometry. As argued in Ref. 73, the ALMO-based definition of the "CT-free" state not only conserves fragment populations (under the Mulliken definition), it also suppresses charge flow between fragments provided that an appropriate polarization subspace (e.g. the one given by Eq. (9)) is chosen for each monomer. Therefore, many orbital rotation degrees of freedom allowed in CDFT are forbidden in an ALMO-based calculation. It is also noteworthy that with a moderately large basis set (def2-TZVPPD[93]), the results given by AO-based ALMO and FERF are fairly

similar for this system. This, however, does not hold for strongly bound donor-acceptor complexes such as NH_3-BH_3,[68] for which diffuse functions need to be removed from the employed basis set to prevent AO-based ALMO from substantially underestimating CT.

From this example we see the first important difference between the ALMO and CDFT definitions of CT: the CDFT definition relies on the existence of net population change, and the contributions from forward and backward donations therefore cancel each other, which is different than the ALMO definition (and other definitions using orbital-space partitioning) in which forward and backward donations contribute in an additive manner. In cases like this the CDFT constraint defining the "CT-free" state is demonstrably too weak, and that state is in fact contaminated with 100% of the energy lowering due to CT.

3.3 Unidirectional H-bonding systems

The next set of H-bonding complexes (X–H$\cdots$Y) we investigate is presumably dominated by donation in one direction (Y to X–H) in terms of the CT effect. Therefore, the mutual cancellation of forward and backward contributions in CDFT should be a less pronounced issue here. The ALMO-EDA results, as well as CT energies calculated by CDFT (with both Becke and FBH population schemes) and energy lowerings due to constant-density relaxation, are collected in Table 3. The total binding energies for the first two complexes are similar to each other, and the contributions from CT, based on the ALMO definition, are also close to each other, accounting for roughly one third of the total binding energy. A similar proportion of CT holds for the water-Cl^- complex, despite the larger magnitude of both the total interaction energy and the CT component due to the existence of an anion.

A rather different picture is given by the CDFT-based approaches. With the CDFT(Becke) method, the resulting CT energies are 67%, 42%, and 87% smaller than the corresponding ALMO results for these systems, respectively. The FBH partitioning scheme yields larger CT energies for this set of systems, especially for the water-Cl^- complex. However, there is

Table 3: Energetic results (in kJ/mol) of ALMO-EDA (using FERFs), CDFT CT, and constant-density (const-ρ) relaxation for three H-bonding systems. All calculations are performed with ωB97X-V/def2-TZVPPD at the equilibrium geometries optimized at the same level of theory.

	H_2O dimer	HF dimer	water-Cl^-
FRZ	-9.40	-7.38	-29.99
POL	-4.59	-5.32	-15.32
CT	-7.16	-6.93	-19.83
Total	-21.15	-19.63	-65.14
CT (CDFT, Becke)	-2.39	-4.03	-2.51
CT (CDFT, FBH)	-3.54	-4.39	-7.85
const-ρ POL	-0.45	-0.30	-0.82
const-ρ CT	-5.05	-4.39	-13.77

still a significant gap compared to the results computed with the ALMO definition.

In order to shed some light on this difference (i.e., is the CDFT constraint defining the "CT-free" state again too weak?), the effect of constant-density relaxation is characterized by performing penalized SCF-MI and SCF calculations as introduced in Sec. 2.3. The energy lowerings are measured against the energy of the frozen wavefunction, and the 3-space density is constrained to be as close to ρ_{frz} as possible. While the effect of const-ρ POL is relatively small, the magnitude of the constant-density interfragment relaxation (CT) suggested by these calculations is striking, although we must note that the imposition of the const-ρ constraint is inexact. For the water dimer and the water-Cl^- complex, the value of const-ρ CT is rather comparable to the gap between ALMO and CDFT CT energies (the energetics for the water dimer is further illustrated in Fig. 4). This finding demonstrates how nature enables intermolecular orbital relaxation without altering the charge population on each fragment (and even the 3-space electron density). Such constant-density intermolecular relaxation is not incorporated in the CDFT definition of CT, as it does not violate the constraint imposed by real-space partitions and thus it already occurs on the "CT-free" state, which explains why CDFT-based approaches usually yield smaller CT energies than orbital-based methods. It is remarkable that in some cases (such as the HF dimer), the

energy lowering due to const-ρ CT is even larger than the difference between the ALMO and CDFT results, which, however, is still possible as long as the system energy after const-ρ relaxation is no lower than that of the CDFT state.

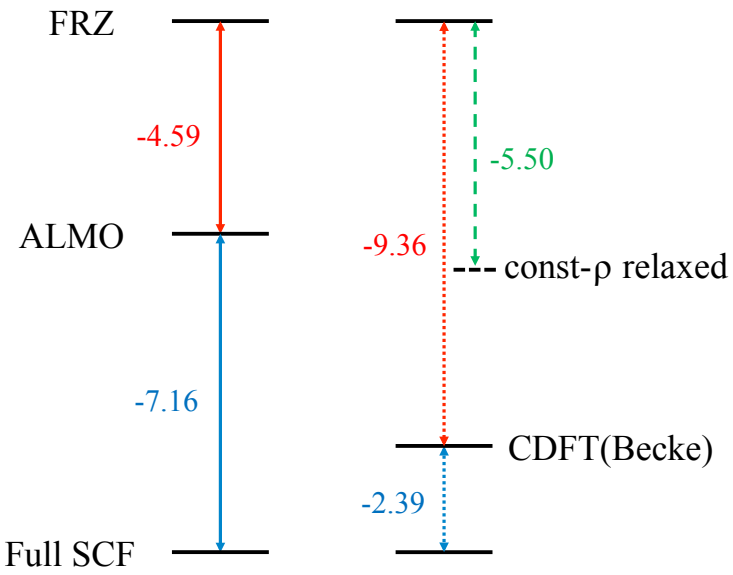

Figure 4: Illustration of the energetics as calculated in Table 3 for the water dimer system. Each horizontal line refers to an intermediate state, and each vertical double-headed arrow corresponds to one type of relaxation, whose associated energy lowering is indicated by the number beside it (in kJ/mol). The dashed horizontal line that is obtained by performing const-ρ relaxation should be close to the energy of the frozen state in DEDA.

Figs. S1–S3 in the Supporting Information demonstrate the distance dependence of FERF- and CDFT-based (with both the Becke and FBH schemes) CT for these H-bonding systems. As identified by the $\log|E_{\mathrm{CT}}|$–R plots, the resulting CT energies decay exponentially with respect to the intermolecular distance. The only exception is CDFT(Becke) for the water-Cl^- complex, where the CT energy turns out to be incorrectly "damped" in the short range.

As mentioned in Sec. 1, the elongation of the X–H bond and the red shift in its stretch frequency are often regarded as fingerprints of CT in typical hydrogen-bonding systems.[9–15] By using the adiabatic EDA, we calculated the CT-induced changes in these two observables,

and the results are shown in Table 4. For the H_2O dimer and the HF dimer, the observable changes calculated by ALMO and CDFT are not remarkably different, and they can be characterized as effects of CT based on the result of either approach. The differences are also consistent with the trend CDFT constraint being slightly weaker than the ALMO constraint.

However, qualitatively different pictures are generated by ALMO and CDFT for the water-Cl^- complex, which is more clearly illustrated in Fig. 5. We note that an adiabatic ALMO-EDA study of this system has been reported in a previous paper by us (Ref. 68), while here we further include the result calculated at the stationary point on the CDFT surface. On the ALMO PES, the optimal structure is roughly midway between the frozen and fully relaxed structures in terms of the $Cl\cdots H_d$ distance and the $Cl\cdot\cdot H_d$–O angle (H_d refers to the donated proton), with a slightly lengthened O–H_d bond compared to that on the frozen PES. It was also revealed that the energy of this structure is extremely close to that of another stationary geometry in which Cl^- lies on the bisector of the H_2O molecule,[68] which further suggests that the near-linear hydrogen bond in the final complex is an effect of CT. The structure optimized on the CDFT PES, in contrast, is rather close to the fully relaxed one, with the O–H_d bond already significantly elongated by 0.02 Å. The red shift in the OH_d stretch frequency, which can be measured by its difference relative to the symmetric stretch frequency of an isolated H_2O (denoted as $\Delta\nu$ in Fig. 5), is also much more significant on the CDFT PES compared to the POL-induced shift calculated by ALMO. As these fingerprints of CT already appear on the PES that is supposed to be "CT-free", the CDFT approach thus suggests a minimal effect of CT on the observable shifts in the water-Cl^- complex. Or, stated another way, the "CT-free" CDFT state is in fact significantly CT-contaminated, akin to formic acid dimer case.

Table 4: X–H bond lengths (Å) and XH stretch frequencies (cm^{-1}) for H-bonding systems X–H$\cdots$Y calculated on the frozen, ALMO, CDFT(Becke), and fully relaxed PES using ωB97X-V/def2-TZVPPD. In order to decouple the two FH modes in the HF dimer, the non-H-bonded hydrogen is substituted with deuterium. For the frozen structure of $H_2O{\cdot}{\cdot}Cl^-$, the lower (symmetric) OH stretch frequency is reported.

	H_2O dimer		HF dimer		$H_2O{\cdot}{\cdot}Cl^-$	
	r_{OH}	ν_{OH}	r_{FH}	ν_{FH}	r_{OH}	ν_{OH}
FRZ	0.961	3861	0.922	4120	0.962	3866
ALMO	0.962	3853	0.923	4095	0.968	3803
CDFT(Becke)	0.964	3829	0.924	4086	0.981	3551
Full	0.967	3754	0.928	3981	0.987	3406

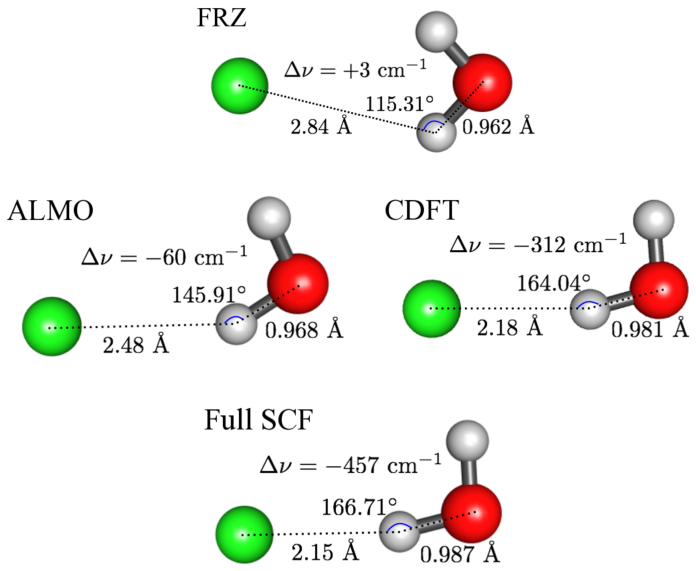

Figure 5: Adiabatic EDA results for the $H_2O\cdots Cl^-$ complex computed with ωB97X-V/def2-TZVPPD. Changes in the Cl$\cdots$H$_d$ distance, the Cl$\cdot\cdot$H$_d$–O angle, length of the O–H$_d$ bond, and the shift ($\Delta\nu$) in the OH$_d$ stretch frequency relative to the symmetric OH stretch of the isolated water monomer (3863 cm^{-1}) are indicated in the figure. Two definitions of the polarized yet "CT-free" state (ALMO and CDFT(Becke)) are compared.

3.4 Borane compounds

Borane (BH_3), as a typical Lewis acid because of its electron-deficient property, can form donor-acceptor complexes with Lewis bases (electron-donating species). The ammonia-borane (NH_3-BH_3) and the borane-carbonyl (BH_3-CO) complexes are two textbook examples for Lewis acid-base adducts, and they have been investigated by various approaches such as the first-generation ALMO-CTA[51] and the regularized SAPT method.[4] Here we revisit these two systems to further explore the differences between the ALMO and CDFT definitions. According to the ALMO-CTA results calculated with ωB97X-V and the slightly smaller def2-TZVPP[94] basis (Table 5), the CT effect in NH_3-BH_3 is dominated by the forward donation towards BH_3, while in the case of BH_3-CO, there is a significant contribution from the back-donation (BH_3 $\rightarrow$CO), which was characterized as from the B–H σ bonds to the π^* anti-bonding orbital of CO by an analysis using the complementary occupied-virtual pairs (COVPs).[51] Therefore, we expect that the CT stabilization energy given by CDFT is small for the BH_3-CO complex due to the mutual cancellation of forward and backward donations under this definition.

Table 5: ALMO-CTA results for NH_3-BH_3 and BH_3-CO complexes calculated with ωB97X-V/def2-TZVPP. The energy changes (ΔE) are in kJ/mol, and the charge delocalizations (ΔQ) are in me^-. For both complexes, "D$\rightarrow$A" refers to the donation towards BH_3, and "A$\rightarrow$D" is for the opposite direction. The high-order (HO) contribution stands for the difference between CT energies calculated by performing a single Roothaan step (RS) and by converging the full SCF solution, which is not further decomposed into D$\rightarrow$A and A$\rightarrow$D contributions.

	D$\rightarrow$A		A$\rightarrow$D		ΔE_{HO}
	ΔE	ΔQ	ΔE	ΔQ	
NH_3-BH_3	-106.60	34.75	-9.58	4.02	-24.14
BH_3-CO	-85.83	22.02	-60.22	41.87	-45.30

The results in Table 6 are consistent with our expectation. For the BH_3-CO complex, the CT energy given by CDFT is close to zero with either population scheme, indicating the near-perfect cancellation of the σ donation of CO with the $\sigma \rightarrow \pi^*$ back donation from BH_3

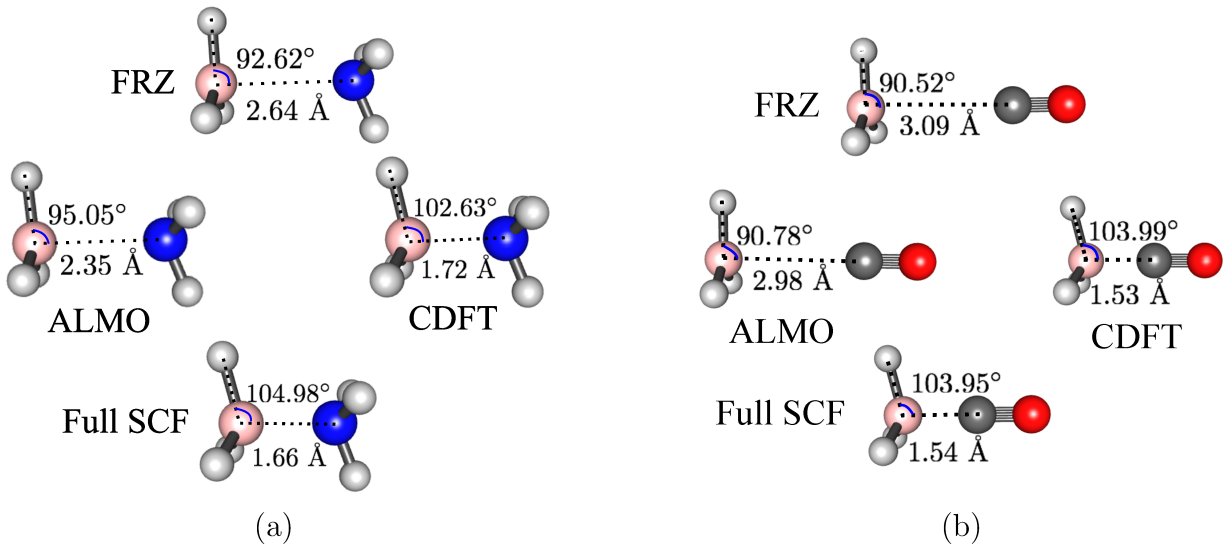

Figure 6: Adiabatic EDA results for the (a) NH_3-BH_3 and (b) BH_3-CO complexes calculated with ωB97X-V/def2-TZVPP. The B$\cdots$Y distance and $\angle$Y$\cdot\cdot$B–H at each equilibrium structure are denoted (Y refers to the atom on the Lewis base that the donating lone pair is associated with). Two definitions of the polarized yet "CT-free" state (ALMO and CDFT(Becke)) are compared.

in terms of the resulting population change in the 3-space. The ALMO-based definition, on the other hand, suggests a substantial contribution from CT, as the forward and backward donations contribute to the total ALMO CT energy in an additive manner. Unlike BH_3-CO, the CT energies given by CDFT gain much larger magnitude for the NH_3-BH_3 complex due to the unidirectionality of its electron donation, which, however, is only about 1/3 as large as the ALMO CT energy. Note that the CT energy for NH_3-BH_3 calculated by CDFT(FBH) is in good agreement with the value reported in Ref. 60 using the same population scheme (-11.99 kcal/mol, calculated by PBE/def2-QZVPPD). This large difference between ALMO and CDFT CT energies, again, is fairly comparable to the magnitude of const-ρ CT: if we use the average of the Becke and FBH results to represent the CDFT value, then const-ρ CT accounts for 87% of the gap between ALMO and CDFT results. In this sense, the NH_3-BH_3 complex is similar to the unidirectional H-bonding systems discussed in Sec. 3.3. Despite the even larger const-ρ CT in BH_3-CO, it is far from addressing the difference between the ALMO and CDFT results for this system, implying that the above-mentioned cancellation

of bidirectional donations should be the more important reason.

Table 6: Energetic results (in kJ/mol) of ALMO-EDA (using FERFs), CDFT CT, and constant-density (const-ρ) relaxation for the NH_3-BH_3 and BH_3-CO complexes. All calculations are performed with ωB97X-V/def2-TZVPPD at the equilibrium geometries optimized at the same level of theory.

	NH_3-BH_3	BH_3-CO
FRZ	117.29	302.13
POL	-150.91	-187.20
CT	-155.88	-278.81
Total	-189.50	-163.88
CT (CDFT, Becke)	-63.62	-0.64
CT (CDFT, FBH)	-52.63	-0.56
const-ρ POL	-20.09	-34.19
const ρ CT	-85.23	-153.84

There is a significant difference between the variational CT energies reported in Table 5 (the sum of D→A, A→D, and HO contributions for the AO-based ALMO method) and Table 6 (the FERF-nDQ method) for the BH_3-CO complex (190 vs. 280 kJ/mol). The agreement is notably better (140 vs 156 kJ/mol) for the NH_3-BH_3 complex, for which the optimized geometry has a longer contact distance (R_{BN} = 1.66 Å vs R_{BC} = 1.54 Å). The agreement was even better for the weaker H-bonding complexes discussed earlier, as shown in Table 2. There are two possible explanations for the significant discrepancy between ALMO/def2-TZVPP and FERF-nDQ/def2-TZVPPD for BH_3-CO. The first possibility is that the AO-based ALMO scheme has underestimated the "true" CT energy because the "CT-free" state is CT-contaminated. Such underestimates clearly occur in larger basis sets with diffuse functions, as illustrated in Ref. 61, while the FERF-nDQ model, on the other hand, exhibits a more stable basis set limit for the CT energy, as verified in Table S2 of the Supporting Information. The def2-TZVPP basis does not have diffuse functions, but CT-contamination may nonetheless occur at the very short 1.54 Å contact distance. However, a second possible explanation is that at such short contacts, the FERF-nDQ set of polarization

functions is not fully adequate to describe polarization, leading to overly large CT values due to underpolarization in the "CT-free" state. In Table S2, we also show POL and CT energies calculated by the "FERF-nDQO" model, where the octupole (O) response functions are also utilized to construct each fragment's polarization subspace. While its basis set convergence behavior is similar to that of FERF-nDQ, the resulting polarization energies are much more favorable and correspondingly the CT energies become smaller than the FERF-nDQ results. For now, we can roughly associate the difference among these models with an uncertainty in the separation of POL and CT in this strongly interacting case, but this question may warrant further investigation in the future.

It was pointed out in Ref. 68 that conventional ALMO-EDA calculations performed at the fully relaxed geometry of a strong donor-acceptor complex often result in a strongly repulsive FRZ term and an overemphasized role of POL, due to the small intermolecular distance driven by the significant CT effect. This seems to be the case for the results in Table 6, and thus it is useful to revisit these systems with the adiabatic EDA. While the full adiabatic EDA results for NH_3-BH_3 and BH_3-CO (including the energetics) are available in the Supporting Information (Table S3), the key features are exhibited in Fig. 6. Since the AO-based ALMO definition is used in these calculations, the def2-TZVPP basis which contains no diffuse functions is employed. Based on the ALMO definition, the significance of polarization is less pronounced under the adiabatic picture, and the key geometric features of these donor-acceptor complexes, including the bending of the originally planar BH_3 molecule (the hybridization of the boron atom changes from sp^2 to sp^3) and the short intermolecular distance, are mainly attributed to CT. These structural features, however, already appear in the CDFT-optimized geometries for both systems. It is clearly revealed in Fig. 6 that while the structures optimized on the ALMO PES are closer to the frozen structures, those optimized with CDFT are more similar to the fully relaxed structures. For BH_3-CO, the CDFT-optimized structure even "overshoots" the fully relaxed one by having

a slightly shorter B$\cdots$C distance and a more bent BH_3 plane. Although this does not go against any basic principles in adiabatic EDA, it is a peculiar result especially for a strong donor-acceptor complex like BH_3-CO. We think that it is most likely related to the specific partitioning scheme (Becke) employed here: the equilibrium geometry optimized with CDFT(FBH) (using finite-difference gradient) has r(B$\cdot\cdot$C) = 1.55 Å and $\angle$C$\cdot\cdot$B–H = 103.77°, which look more reasonable in comparison.

3.5 Metal-carbonyl complexes

Metal-carbonyl complexes are another important class of donor-acceptor adducts whose charge-transfer effects have been previously studied by approaches such as CSOV,[95] BLW-EDA,[49] and ALMO-CTA.[51] Based on the change in CO stretch frequency upon the complexation, they can be categorized into "classical" (whose ν(CO) is red-shifted) and "nonclassical" (ν(CO) blue-shifted) metal-carbonyl complexes.[96,97] According to the ALMO- or BLW-based analyses,[49,51] the classification is determined by the relative strength of the backward donation (M(d)$\rightarrow$CO(π^*)) and the forward donation that forms the σ(M–C) bond.

Here we choose two simple monocarbonyl complexes $Cu(CO)^+$ and Ni(CO) that were previously investigated by Mo et al.[49] to show the difference in ALMO and CDFT results, which, according to Table 7 in Ref. 49, are representative of the above-mentioned "nonclassical" and "classical" cases, respectively. In order to verify that our previous findings still hold upon a change of functional, and to compare with the results in Ref. 49, the B3LYP functional[98] with a Becke-Johnson damped D3 correction[99] is employed for this set of calculations. The energetic results computed at the equilibrium structures are summarized in Table 7. The ALMO-EDA results suggest that POL is the most significant binding force for the $Cu(CO)^+$ complex, while Ni(CO) is more similar to the borane complexes (see Table 6) whose FRZ and POL both have very large magnitude but are of opposite signs (due to the close intermolecular contact). The CT component, nevertheless, still has the largest

contribution to the latter system . Note that the ALMO-EDA results here are remarkably different from the BLW-EDA results presented in Ref. 49: the CT energies reported in the latter are much larger for both systems, and the POL components are correspondingly smaller. The reason for this difference is unclear to us, as the FERF model employed in our calculations, by construction, should yield even larger CT energies than those obtained by using the original ALMO model, where the latter is formulated in the same way as the BLW approach.

The CDFT-based CT energies, on the other hand, are roughly one order of magnitude smaller than the ALMO results for both systems, although the relative strength of CT between these two complexes is correctly reflected. This is most likely because the forward (σ) and backward ($d \rightarrow \pi^*$) donations are both not negligible in these complexes, as suggested in Refs. 49 and 51, and they cancel each other under the CDFT definition.

Table 7: ALMO-EDA (using FERFs) and CDFT results (in kJ/mol) for the $Cu(CO)^+$ and Ni(CO) model complexes. All calculations are performed with B3LYP-D3(BJ)/def2-TZVPPD at the equilibrium geometries optimized at the same level of theory. The spin state of the Ni atom remains singlet throughout, i.e., the energy consumed for the spin-state promotion is not included.

	$Cu(CO)^+$	Ni(CO)
FRZ	12.75	171.41
POL	-128.50	-220.11
CT	-48.60	-232.97
CT (CDFT, Becke)	-8.54	-32.79
CT (CDFT, FBH)	-5.62	-37.69
INT	-164.35	-281.67

The significance of the M→CO backward donation can be revealed from the shift in CO stretch frequency (ν(CO)) relative to that for an isolated CO molecule. Here we utilize the adiabatic EDA approach again to track the changes in ν(CO) and the M–C and C–O distances, and the results are summarized in Table 8. On the frozen PES, ν(CO) is shifted to a higher frequency and the length of the C–O bond is reduced. These changes

Table 8: Summary of adiabatic EDA results for $Cu(CO)^+$ and Ni(CO) computed with B3LYP-D3(BJ)/def2-TZVPP. The distances are in Å and the vibrational frequencies are in cm^{-1}. The Ni(CO) complex remains to be singlet at all stages.

	$Cu(CO)^+$			Ni(CO)		
	R(M–C)	R(C–O)	ν(CO)	R(M–C)	R(C–O)	ν(CO)
FRZ	2.328	1.112	2338	2.831	1.123	2231
ALMO	2.027	1.111	2362	1.923	1.117	2321
CDFT	1.858	1.116	2320	1.729	1.136	2192
Full SCF	1.905	1.114	2314	1.678	1.148	2090
Free CO		1.125	2215			

are substantial for the cationic $Cu(CO)^+$ complex while being much smaller for the neutral Ni(CO) system whose optimal M–C distance on the frozen PES is also over 0.5 Å larger. We note that the blue shift in CO stretch frequency on the frozen surface is an interesting finding provided by the adiabatic ALMO-EDA, and it might be related to other phenomena such as blue-shifting hydrogen bonds,[81,100,101] although a detailed analysis of this is obviously beyond the scope of the present paper. Polarization, as suggested by the ALMO model, further shortens the C–O bond and gives rise to an increased blue shift. The final ν(CO) is thus determined by CT: for the "classical" complex Ni(CO), ν(CO) is lowered by ∼230 cm^{-1} once CT is enabled, indicating a significant M(d)→CO(π^*) donation and rendering an eventually red-shifted ν(CO) (by 125 cm^{-1}) and a lengthened C–O bond (by over 0.02 Å); for the "nonclassical" complex $Cu(CO)^+$, the effect of CT is much smaller and ν(CO) is still blue-shifted by roughly 100 cm^{-1} on the fully relaxed surface.

In contrast, on the "CT-free" PES defined based on CDFT, ν(CO) is already lower than the frequency of free CO stretch and the C–O bond is also elongated, suggesting a rather different role of CT in modulating the properties of Ni(CO). The CDFT results for $Cu(CO)^+$ are even more extraordinary, as the resulting optimized geometry "overshoots" the fully relaxed structure by having a shorter R(Cu–C) and a longer C–O bond. The resulting ν(CO) is very close to the full SCF result as well. These results indicate that the M→CO

donation already occurs on the CDFT surface, which thus seems to be an inappropriate definition for the "CT-free" state at least for the metal-carbonyl complexes.

3.6 Complexes of water and metal cations

The last set of systems that we investigate in this section comprises five complexes formed by water and alkali (Li, Na, K) or alkali earth (Mg, Ca) metal cations. A separation of POL and CT for these interactions is meaningful for the development of polarizable force fields, as shown in several works by us[90,102] and others.[103–105] Using the second-generation ALMO-EDA, it was found that the magnitude of the equilibrium CT energies for these systems is ordered as Na < K < Li and Mg < Ca,[90] and the latter was further manifested through a study using the adiabatic ALMO-EDA.[68] On the other hand, it was reported in Ref. 61 that the CDFT(Becke) approach gives a different order (K < Na < Li) for the monovalent cations, which was considered to be more reasonable for these "obvious" cases as ΔE_{CT} was supposed to be larger with a shorter $\mathrm{O}\cdots\mathrm{M}^{+}$ distance.

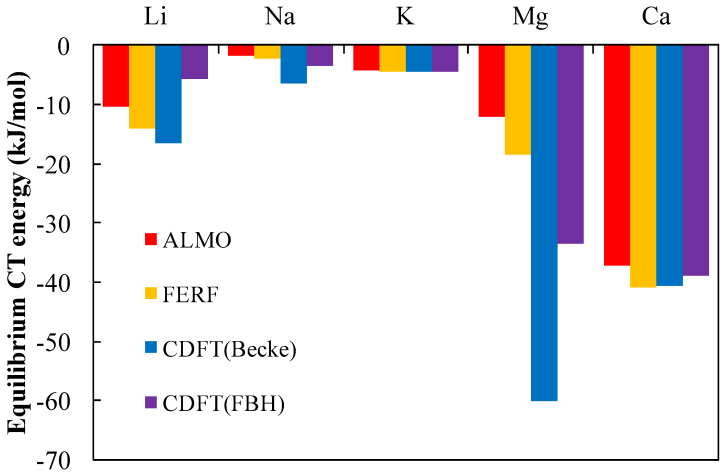

Figure 7: Equilibrium CT stabilization energies (in kJ/mol) for the water-M^{n+} (M^{n+}= Li^{+}, Na^{+}, K^{+}, Mg^{2+} and Ca^{2+}) complexes evaluated using AO-based ALMO (red), FERF (yellow), CDFT(Becke) (blue) and CDFT(FBH) (purple) methods. All the calculations are performed at the ωB97X-D3/def2-QZVPPD level of theory, while the equilibrium structures optimized with ωB97X-V/def2-QZVPPD are from a previous work.[90]

The equilibrium CT energies for these systems evaluated with four distinct models (original AO-based ALMO, FERF-nDQ, CDFT(Becke), and CDFT(FBH)) are plotted in Fig. 7 (the original data are available in Table S4 of the Supporting Information). The ωB97X-D3 functional[106] is employed here in order to compare with the results in Ref. 61. Since a quadruple-ζ basis set (def2-QZVPPD) is used, there is a notable gap between the results of AO-based ALMO (which was used in Ref. 61) and FERF, especially for the complexes of smaller intermolecular distances (water-Li^+, Mg^{2+}). Nonetheless, as opposed to all other systems discussed above, the CT energies given by FERF are still smaller than the CDFT(Becke) results for the complexes with Li^+, Na^+, and Mg^{2+}, while the gap becomes much smaller on K^+ and Ca^{2+} for which the FERF results are marginally more favorable. Fig. 7 also indicates the CDFT results are sensitive to the employed population scheme, as ΔE_{CT} is significantly decreased for the complexes with Li^+ (65%), Na^+ (46%), and Mg^{2+} (44%) once the Becke partitioning scheme is replaced by FBH (the percent values in the parentheses are reductions relative to the CDFT(Becke) values). Interestingly, the CT energies generated by CDFT(FBH) are ordered in the same way as the FERF results, despite the substantial energy differences between these two approaches for $H_2O\cdots Li^+$ and $H_2O\cdots Mg^{2+}$.

While there is no criterion for a unique correct order for the magnitude of CT energies in these systems, it is possible to shed some light on the strikingly large CT energies given by CDFT(Becke) for the water-Mg^{2+} and, to a lesser extent, water-Li^+ complexes. The Becke scheme essentially relies on a partition based on atomic Voronoi cells (although they are shifted to account the difference in atom sizes) to obtain the value of the CDFT weighting function on each grid point, i.e., the 3-space density evaluated on a grid point is assigned to a fragment according to a distance-based criterion. Therefore, for systems whose $O\cdots M^{n+}$ distance is relatively small, such a partitioning scheme that completely neglects the electronic structure might place the interfragment boundary in a region where the electron density of water is not yet insignificant. As a consequence, the polarization of H_2O, which also pulls its

electron density towards the cation, might be misinterpreted as CT across the boundary and thus be incorrectly inhibited in the CDFT(Becke) calculations. Table 9 shows the electron population on H_2O to be constrained based on the Becke partition, which is in line with our assumption. For the complexes with Li^+, Na^+ and Mg^{2+}, the electron population on the H_2O fragment is less than 10, indicating that the Becke scheme divides the system such that a small portion of electron density of H_2O is assigned to the metal cation, which, as we argued above, might lead to an insufficiently polarized CDFT solution. On the other hand, the partitions in water-K^+ and water-Ca^{2+} allow them to be fully polarized in the CDFT calculation, and thus the CDFT(Becke) scheme does not yield excessively large CT energies for these systems. In this sense, FBH seems to be a more advantageous partitioning scheme as it makes use of the electronic structure information in the construction of the weight matrix. It is also noteworthy that modifications to the Becke scheme were proposed[107–109] to adjust the positions of partition cells "more freely" using topological information from the electron density, and it might be useful to consider those partition schemes in CDFT calculations.

Table 9: Number of electrons on the H_2O molecule that are constrained in the CDFT(Becke) calculations for the $H_2O\cdots M^{n+}$ complexes (using ωB97X-D3/def2-QZVPPD). The values are determined by projecting the promolecule 1PDM onto the Becke weight matrix associated with the H_2O fragment.

	Li^+	Na^+	K^+	Mg^{2+}	Ca^{2+}
Population (e^-)	9.84	9.95	10.06	9.88	10.03

Although there is no doubt that the strength of CT is closely related to parameters such as the intermolecular distance, the IP of the donor and the EA of the acceptor, one should not reach a conclusion only based on a subset of them. For instance, it was argued in Ref. 105 that the CT energies for divalent cations should have an order $Mg^{2+} > Ca^{2+}$ as the EA of the former is larger, which, at the same time, is also consistent with the distance-based

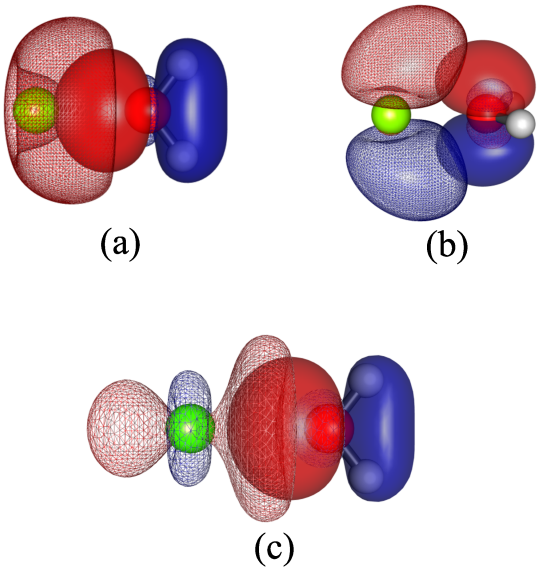

Figure 8: Dominating COVPs for the forward donations ($H_2O \rightarrow M^{n+}$) in the water-Mg^{2+} (a, b) and water-Ca^{2+} (c) complexes generated by the original ALMO-CTA using the smaller def2-SVPD basis. The donor (solid) and acceptor (meshed) orbitals are plotted with an isosurface value 0.05 a.u.

argument in Ref. 61. However, according to Fig. 7, such an ordering is only supported by the CDFT(Becke) scheme. Using the original ALMO-CTA, we plotted the most significant COVPs for the $H_2O \rightarrow Mg^{2+}$ and $H_2O \rightarrow Ca^{2+}$ donations in Fig. 8. Qualitative difference exists in the donor-acceptor orbital pictures for these two systems: for $H_2O \cdots Mg^{2+}$, there are two significant COVPs and the acceptor orbitals on Mg^{2+} are an *sp*-hybridized orbital (in panel a) and an empty *p* orbital (in panel b), respectively; for the complex with Ca^{2+}, there is only one dominant COVP (panel c), and the acceptor orbital is clearly an empty *d* orbital of Ca^{2+}. While the COVP analysis itself does not suffice to rationalize the larger CT energy in $H_2O \cdots Ca^{2+}$ than in $H_2O \cdots Mg^{2+}$, it implies that a simple argument based on the $O \cdots M^{n+}$ distance or the EA of M^{n+} solely may overlook some of the underlying details about CT.

The distance dependence of CT for the water-Na^+ complex calculated with different definitions is exhibited in Fig. 9. It is striking that the CT energies given by both CDFT

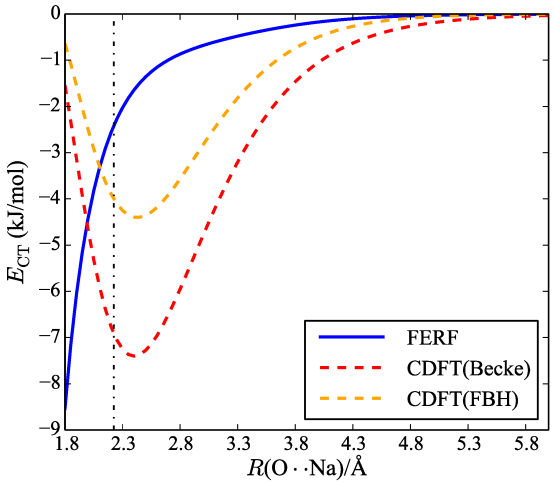

Figure 9: Distance dependence of the CT energies (in kJ/mol) given by the FERF, CDFT(Becke), and CDFT(FBH) models for the $H_2O{\cdot\cdot}Na^+$ complex (computed with ωB97X-V/def2-QZVPPD). The intermolecular $O{\cdot\cdot}Na^+$ distance is modified with an interval of 0.05 Å, while the other degrees of freedom are kept frozen. The vertical dashed lines indicate the equilibrium $O{\cdot\cdot}Na^+$ distance (2.224 Å).

schemes change *non-monotonically*: when the two fragments approach each other, the CT energy becomes most attractive beyond the equilibrium distance, and then becomes less so when the intermolecular separation is further shortened. The FERF-nDQ method, on the other hand, manifests the characteristic exponential decay in the entire plotting range. This non-monotonic behavior of CDFT-based CT also appears for complexes of water with Li^+ and Mg^{2+}, but not for those with K^+ and Ca^{2+} (see Fig. S4 in the Supporting Information for more details). Moreover, we also found non-monotonic behavior in neutral systems such as the NH_3-BH_3 and even the water dimer (in the strongly compressed regime), as illustrated in Fig. S5. We think that the decrease of CDFT-based CT in the short range also originates from the characteristics of real-space partitions: when the donor and acceptor orbitals have a substantial spatial overlap, the CT between them can be associated with little change in the 3-space population, i.e., it can bypass the constraint exerted in CDFT calculations. This also possibly explains why this non-monotonic behavior emerges for $H_2O{\cdot\cdot}Mg^{2+}$ but not for $H_2O{\cdot\cdot}Ca^{2+}$ (at least in the present plotting range): as shown in Fig. 8, the acceptor orbitals

are spatially in closer contact with the donor ones in the former complex, while the dominant acceptor orbital on Ca^{2+}, because of its d character, is more separated from the donor orbital in the 3-space.

3.7 Comparison with the regularized SAPT method

Before concluding this paper, we want to briefly discuss the recently proposed regularized SAPT method,[4] which provides a distinct perspective on CT. In this scheme, CT is considered to be a tunneling process induced by the Coulomb potential of fragment nuclei, as it is not fully screened by the electrons and becomes singular when $r \to 0$. Therefore, by calculating the second-order SAPT(DFT) induction energy with a regularized Coulomb operator that is screened in the short range ($1/r \to (1-\mathrm{e}^{-\eta r})/r$), a "CT-free" induction energy can be obtained. The CT energy can thus be computed in a subtractive way, as shown by Eq. (1). While the formulation of this method is completely different than the ALMO-based definition, they should at least have two common features: (i) the forward and backward contributions are constructive rather than canceling each other, and (ii) the definition of CT does not rely on net charge flow.

Table 10: Comparison of CT energies (in kJ/mol) evaluated with the regularized SAPT, ALMO (using FERF-nDQ), and CDFT approaches. The regularized SAPT results are based on Table 1 in Ref. 4 by combining the second-order D→A and A→D contributions, and the ALMO and CDFT calculations are performed at the ωB97X-V/def2-TZVPPD level of theory. For consistency, geometries provided in the Supporting Information of Ref. 4 are used for these calculations.

	Regularized SAPT		ALMO		CDFT	
	$CT^{(2)}$(total)	$IND^{(2)}$(total)	CT	POL+CT	CT(Becke)	CT(FBH)
H_2O dimer	-1.49	-5.84	-5.53	-9.35	-2.02	-2.89
HF dimer	-1.37	-6.27	-6.82	-12.06	-3.91	-4.27
pyridine dimer	-0.36	-3.26	-3.34	-6.63	0.00	0.00
FH$\cdots$CO	-1.44	-6.47	-9.26	-13.38	-3.21	-3.10
FH$\cdots$OC	-0.39	-3.06	-2.43	-5.29	-1.91	-1.60
NH_3-BH_3	-71.49	-175.60	-142.97	-277.44	-64.79	-55.58
BH_3-CO	-171.01	-346.69	-284.45	-477.64	-0.33	-1.13

With the same set of systems as in Table 1 of Ref. 4, we compare the equilibrium CT

energies evaluated with the regularized SAPT, ALMO, and CDFT definitions in Table 10. We note that for systems that were investigated above, the ALMO and CDFT results are slightly different here, as the geometries are directly taken from Ref. 4. The contrast between the ALMO and CDFT results is consistent with the trends that have been elucidated via the examples above, and it is notable that the pyridine dimer (C_{2h}), as another cyclic H-bonding complex, has zero CT according to the CDFT definition, which is clearly not the case for regularized SAPT.

However, for all complexes investigated in Table 10, the regularized SAPT method yields a smaller CT energy compared to the corresponding ALMO result; and for the unidirectional H-bonding systems (the first four complexes), its magnitude is even smaller than that of the corresponding CDFT result. We think that the relatively small magnitude of regularized SAPT CT energies might arise from the truncation of SAPT induction energy at the second-order: for each complex in Table 10, the total pairwise additive second-order induction energy, $\mathrm{IND}^{(2)}$(Total), is significantly smaller than the sum of POL and CT suggested by ALMO-EDA. Recall that within the SAPT(DFT) theory, a "δHF" term (defined as the difference between the counterpoise-corrected Hartree-Fock interaction energy and the second-order SAPT energy excluding the dispersion and exchange-dispersion terms) is utilized to capture the missing high-order induction effect. With this term taken into account, the total SAPT(DFT) induction energy for the equilibrium water dimer, the first system in Table 10, was reported to be -2.2840 kcal/mol (-9.56 kJ/mol),[110] which is in fairly good agreement with the "POL+CT" value given by ALMO-EDA. Moreover, it was suggested by Řezáč et al. that the δHF term contains a significant contribution from CT as it manifests a good correlation with CT energies computed with CDFT(FBH),[60] which further supports our perspective that the relatively small magnitude of regularized SAPT CT is at least partly caused by not taking the δHF term (high-order induction effect) into account in the formulation of this theory. We note that the necessity of including CT beyond second-order was also

pointed out by Misquitta in the original regularized SAPT paper (Ref. 4). In a more recent work regarding the construction of intermolecular potentials for the pyridine dimer,[111] it was suggested that its magnitude could be estimated by using a classical polarization model based on distributed multipoles and polarizabilities.

Table 11: Comparison of the forward (D→A) and backward (A→D) CT energies (in kJ/mol) given by regularized SAPT and ALMO-CTA. The regularized SAPT results are taken from Table 1 in Ref. 4, and the ALMO-CTA results are calculated with the Roothaan-step (RS)-based scheme introduced in Ref. 51 using the original AO-based ALMO definition. The high-order (HO) contribution is defined in the same way as in Table 5. The ωB97X-V/def2-TZVPPD level of theory is employed for the first five complexes, while the less diffuse def2-TZVPP basis set is used for the two BH_3-containing complexes.

	Regularized SAPT		ALMO-CTA (AO-based)		
	CT(D→A)	CT(A→D)	CT(D→A)	CT(A→D)	HO
H_2O dimer	-1.39	-0.10	-4.06	-0.23	-0.94
HF dimer	-1.33	-0.04	-5.20	-0.25	-1.09
pyridine dimer	-0.18	-0.18	-1.20	-1.20	-0.47
$FH\cdots CO$	-1.39	-0.05	-6.32	-0.43	-1.56
$FH\cdots OC$	-0.37	-0.02	-1.69	-0.21	-0.33
NH_3-BH_3	-61.65	-9.84	-101.15	-7.51	-23.54
BH_3-CO	-139.16	-31.85	-85.82	-63.48	-46.76

As a scheme utilizing orbital-space partitioning, the regularized SAPT approach by construction provides a decomposition of the CT energy into forward and backward contributions at the second order. Table 11 compares such decompositions given by the regularized SAPT and the original ALMO-CTA[51] approaches. Despite the substantial differences in the magnitude of CT energies, the relative significance of forward and backward CT given by these two methods qualitatively agree with each other, except for the BH_3-CO complex where ALMO-CTA suggests a more pronounced back donation from BH_3. We note that the AO-based definition of ALMOs is employed to generate the results in Table 11, as the extension of ALMO-CTA to SCF-MI solutions using FERFs is currently still under development due to the complication arising from the excluded virtual orbitals on each fragment. The CDFT-based definition, on the other hand, is *not* able to separate the forward and backward

contributions with its present formulation.

4 Conclusion

In this paper, we have conducted a thorough study of the definitions of CT in the context of intermolecular interactions. The performance of the ALMO- and CDFT-based approaches, which represent definitions based on orbital- and real-space partitions, respectively, is investigated and compared on a wide range of model systems concerning the energetic stabilization effect (ΔE_{CT}) as well as the observable consequences. Techniques recently developed by us, such as the constant-density SCF-MI/SCF calculations and the adiabatic EDA scheme (the latter is extended to CDFT in this work), are utilized in this study to provide useful information. The main findings are summarized as follows:

- The CDFT definition concerns the net charge flow between molecules, while the ALMO and many other orbital-based definitions regard CT as an intermolecular orbital relaxation effect. Therefore, the "CT-free" state obtained via CDFT can be contaminated by energy lowering due to intermolecular relaxation as long as forward and backward donations shift equal fractions of an electron. This effect is most pronounced for the cyclic H-bonding systems where the transfers in two ways exactly cancel each other because of symmetry, and it is also revealed in other systems (BH_3-CO, Ni(CO)) that involve significant back-donation.

- Significant intermolecular relaxation can take place without changing the fragment populations, i.e., the variational principle is able to work around the constraints in a CDFT calculation. This is revealed by calculating the constant-density CT energy, for which a 3-space density constraint that is stricter than the requirement of conserving fragment populations is applied. Such an effect explains why CDFT usually gives smaller CT energies than ALMO's even for systems whose CT is presumably unidirectional, as illustrated

by examples such as the H_2O dimer and the NH_3-BH_3 complex. It may also be responsible for the non-monotonic distance dependence of CDFT-based CT in the overlapping regime.

- The above two differences extend to the observable consequences of CT calculated with the ALMO and CDFT definitions. It is a probable signature of CT-contamination that many well-established fingerprints of CT, such as the red shift in water's OH stretch frequency when it is bound to Cl^-, and the bending of the planar BH_3 upon the formation of donor-acceptor complexes, already appear in the "CT-free" state constructed by CDFT. On the other hand, the changes in these observables are characterized as effects of CT through adiabatic EDA calculations using the ALMO definition.

- There exist special cases where CDFT yields larger CT energies than the ALMO results. In the cases of water-Mg^{2+}, Li^+, Na^+ complexes examined above, the CDFT results showed a strong dependence on the choice of population scheme. Evidence was provided that CDFT with the original Becke partition, which yields anomalously large values of CT, are likely to be inappropriate for these cases.

Certainly the CDFT-based definition has a number of desirable features. For instance, the CT energies calculated by CDFT are fairly insensitive to the employed basis set, which is an advantage over earlier orbital-based approaches. From the practical perspective, the CDFT definition of CT might be favored for the development of molecular force fields, as it is clearly difficult to use an empirical function to model a term of large magnitude concerning quantum delocalization effect. CT energies computed by CDFT, in principle, should be better correlated with net population change upon complexation, where the latter can be measured for certain systems by experimental means.[112]

The results of this paper highlight the fact that the ALMO and CDFT definitions of CT capture different physics. The CDFT condition prohibits net population transfer between

fragments, and thus its constrained "CT-free" state is demonstrably CT-contaminated in any system where CT can occur without net population change. The ALMO-based definition aims to prohibit all intermolecular orbital mixing, and therefore is more consistent with the common understanding of CT effects in chemistry, especially in terms of the calculated observable consequences of CT. The recently proposed FERF-nDQ approach has a stable basis set limit for the resulting CT energy while retaining the preferable features of the ALMO definition. Based on these facts, as well as the generally satisfactory agreement between polarization energies evaluated by FERF-nDQ and AO-based ALMO in compact basis sets, it can be recommended for characterizing the effects of CT in non-covalently bound systems despite the uncertainty mentioned in Sec. 3.4 that still needs to be resolved for strong dative complexes. Development of the associated theoretical tools, such as a pairwise CT analysis scheme (which is analogous to the original ALMO-CTA[51]) and the analytical nuclear gradient for the "SCF-MI(FERF)" PES (for performing adiabatic EDA), will be highly desirable, and we hope to report progress on these problems in the future.

Associated Content

Supporting Information

Full adiabatic EDA results for the formic acid dimer and BH_3 complexes (NH_3-BH_3 and BH_3-CO); basis set convergence of POL and CT energies computed by AO-based ALMO and FERF-nDQ; original data for the CT energies plotted in Fig. 7 (PDF); equilibrium geometries of systems investigated in this work (ZIP).

Acknowledgments

This work was supported by grants CHE-1665315 and CHE-1363342 from the U.S. National Science Foundation (NSF). The authors thank Dr. Yihan Shao (University of Oklahoma) for technical support on the implementation of the fragment-based Hirshfeld population scheme in the Q-Chem software package.

A Nuclear gradient for the CDFT(Becke) approach

In the derivation presented below, we use μ, ν,... for AO basis indices, i, j,... for occupied MO indices, a, b,... for virtual MO indices, and p, q,... for generic (occupied or virtual) MO indices. Tensorial notations are used following the same convention as in our previous papers (e.g. Ref. 45).

The energy functional given by Eq. (13) can be rewritten using the 1PDM:

$$E[\mathbf{P}] = E_0[\mathbf{P}] + \sum_A \lambda_A \,\mathrm{Tr}[(\mathbf{P} - \mathbf{P}_0)\mathbf{W}_A] \tag{16}$$

where E_0 is the standard KS energy, $\mathbf{W}_A$ is the weight matrix as defined in Eq. (12), and $\mathbf{P}_0$ is the promolecule density matrix that has a fragment-block-diagonal structure:

$$(P_0)^{A\mu A\nu} = \sum_i (C_o)^{A\mu}_{\ \ Ai} (C_o^T)^{\ A\nu}_{Ai} \tag{17}$$

Differentiating both sides of Eq. (16) with respect to nuclear positions (x), we get

$$\begin{aligned} E^x = E_0^x &+ \sum_A \lambda_A \,\mathrm{Tr}[(\mathbf{P} - \mathbf{P}_0)\mathbf{W}_A^x] \\ &- \sum_{A=1}^{N_{\mathrm{frgm}}} \left(\frac{\partial \mathbf{P}_0}{\partial \mathbf{S}_A} \cdot \mathbf{S}_A^x + \frac{\partial \mathbf{P}_0}{\partial \boldsymbol{\theta}_A} \cdot \boldsymbol{\theta}_A^x \right) \cdot \mathbf{W}_{\mathrm{sum}} \end{aligned} \tag{18}$$

where $\mathbf{S}_A$ and $\boldsymbol{\theta}_A$ refer to the AO overlap matrix and the orbital rotation matrix ($n_v \times n_o$) for fragment $\mathbf{A}$, respectively, and

$$\mathbf{W}_{\text{sum}} = \sum_A \lambda_A \mathbf{W}_A \tag{19}$$

The first term on the RHS of Eq. (18) is the standard KS-DFT gradient, which has been well-documented in literature,[113] and the second term represents the change in the CDFT weight matrices with respect to the nuclear displacement, which can be obtained by modifying the routines available in Q-Chem that evaluate the XC contribution to the gradient, as the second term on the RHS of Eq. (16) is essentially an local density approximation (LDA)-like functional. The third term, which reflects the response of the promolecule density, is more challenging to evaluate. Starting from Eq. (17), we first parameterize $C^{A\mu}_{\ \ Ai}$ with $\mathbf{S}_A$ and $\boldsymbol{\theta}_A$:

$$\begin{aligned} C^{A\mu}_{\ \ Ai} = C^{A\mu}_{\ \ As} (S_A^{-\frac{1}{2}})^{As}_{\ \ Ar} \big[&\delta^{Ar}_{\ \ Ai} + (\theta_A)^{ArAs} \delta_{AsAi} \\ &- (\theta_A)^{AsAr} \delta_{AsAi} + \mathcal{O}(\boldsymbol{\theta}_A^2) \big] \end{aligned} \tag{20}$$

Therefore, we have

$$\begin{aligned} &\sum_{A=1}^{N_{\text{frgm}}} (W_{\text{sum}})_{A\mu A\nu} \frac{\partial P_0^{A\mu A\nu}}{\partial S_{A\lambda A\sigma}} S^x_{A\lambda A\sigma} \\ &= \sum_{A=1}^{N_{\text{frgm}}} -\frac{1}{2} \left(C^{A\mu}_{\ \ As} C^{A\lambda}_{\ \ As} S^x_{A\lambda A\sigma} C^{A\sigma}_{\ \ Ai} C^{A\nu}_{\ \ Ai} + \text{c.c.} \right) (W_{\text{sum}})_{A\mu A\nu} \\ &= \sum_{A=1}^{N_{\text{frgm}}} -\frac{1}{2} \left[(\mathbf{S}_A^{-1}) \mathbf{S}_A^x \mathbf{P}_A + \mathbf{P}_A \mathbf{S}_A^x (\mathbf{S}_A^{-1}) \right] \cdot \mathbf{W}_{\text{sum},A} \end{aligned} \tag{21}$$

and

$$\begin{aligned}
&\sum_{A=1}^{N_{\mathrm{frgm}}} (W_{\mathrm{sum}})_{A\mu A\nu} \frac{\partial P_0^{A\mu A\nu}}{\partial \theta^{AaAi}} (\theta^x)^{AaAi} \\
&= \sum_{A=1}^{N_{\mathrm{frgm}}} (W_{\mathrm{sum}})_{A\mu A\nu} (C_{Aa}^{A\mu} C_{Ai}^{A\nu} + C_{Ai}^{A\mu} C_{Aa}^{A\nu}) (\theta^x)^{AaAi} \\
&= 2 \sum_{A=1}^{N_{\mathrm{frgm}}} (W_{\mathrm{sum}})_{AaAi} (\theta^x)^{AaAi} \\
&= 2 \sum_{A=1}^{N_{\mathrm{frgm}}} \mathbf{W}_{\mathrm{sum},A}^{(\mathrm{vo})} \cdot \boldsymbol{\theta}_A^x
\end{aligned} \tag{22}$$

The RHS of Eq. (22) can be computed using the z-vector approach,[114] i.e., based on the stationary condition of SCF calculations for isolated fragments, we have

$$\begin{aligned}
\mathbf{W}_{\mathrm{sum},A}^{(\mathrm{vo})} \cdot \boldsymbol{\theta}_A^x = \mathbf{z}_A \cdot \Big(& E_A^{\boldsymbol{\theta}_A \mathbf{h}_A} \cdot \mathbf{h}_A^x + E_A^{\boldsymbol{\theta}_A \mathbf{II}_A} \cdot \mathbf{II}_A^x \\
& + E_A^{\boldsymbol{\theta}_A \mathbf{S}_A} \cdot \mathbf{S}_A^x + E_{\mathrm{xc},A}^x \Big)
\end{aligned} \tag{23}$$

where $\mathbf{h}_A$ is fragment A's core Hamiltonian, and $\mathbf{II}_A$ refers to its two-electron AO integrals. The z-vector, $\mathbf{z}_A$, is the solution to the following linear equation:

$$E_A^{\boldsymbol{\theta}_A \boldsymbol{\theta}_A} \mathbf{z}_A = \mathbf{W}_{\mathrm{sum},A}^{(\mathrm{vo})} \tag{24}$$

where $E_A^{\boldsymbol{\theta}_A \boldsymbol{\theta}_A}$ is the orbital Hessian for the KS energy of fragment A. The contraction of the z-vector with the quantity in the parenthesis in Eq. (23) involves rather complicated equations, and we refer the reader to the ESI of our previous paper (Ref. 68) for the full details.

We note that the nuclear gradient derived above should have been comprised in the gradient for the CDFT configuration interaction (CI) theory reported by Kaduk et al.[115]

Nonetheless, for the special case where only one single determinant is involved, the form given above is much easier to understand and convenient for implementation purpose.

References

(1) Stone, A. *The Theory of Intermolecular Forces*; Oxford University Press, 2013.

(2) Marcus, R. A. *Rev. Mod. Phys.* **1993**, *65*, 599.

(3) Newton, M. D. *Chem. Rev.* **1991**, *91*, 767–792.

(4) Misquitta, A. J. *J. Chem. Theory Comput.* **2013**, *9*, 5313–5326.

(5) Hammerum, S. *J. Am. Chem. Soc.* **2009**, *131*, 8627–8635.

(6) Mizuse, K.; Hasegawa, H.; Mikami, N.; Fujii, A. *J. Phys. Chem. A* **2010**, *114*, 11060–11069.

(7) Attah, I. K.; Platt, S. P.; Meot-Ner, M.; El-Shall, M. S.; Peverati, R.; Head-Gordon, M. *J. Phys. Chem. Lett.* **2015**, *6*, 1111–1118.

(8) Peverati, R.; Platt, S. P.; Attah, I. K.; Aziz, S. G.; El-Shall, M. S.; Head-Gordon, M. *J. Am. Chem. Soc.* **2017**, *139*, 11923–11932.

(9) Szczepaniak, K.; Tramer, A. *J. Phys. Chem.* **1967**, *71*, 3035–3039.

(10) Ratajczak, H. *J. Phys. Chem.* **1972**, *76*, 3000–3004.

(11) Thompson, W. H.; Hynes, J. T. *J. Am. Chem. Soc.* **2000**, *122*, 6278–6286.

(12) Alabugin, I. V.; Manoharan, M.; Peabody, S.; Weinhold, F. *J. Am. Chem. Soc.* **2003**, *125*, 5973–5987.

(13) Ramos-Cordoba, E.; Lambrecht, D. S.; Head-Gordon, M. *Faraday Discuss.* **2011**, *150*, 345–362.

(14) Weinhold, F.; Klein, R. A. *Mol. Phys.* **2012**, *110*, 565–579.

(15) Wang, C.; Danovich, D.; Shaik, S.; Mo, Y. *J. Chem. Theory Comput.* **2017**, *13*, 1626–1637.

(16) Bader, R. *Can. J. Chem.* **1964**, *42*, 1822–1834.

(17) Liu, S. Y.; Dykstra, C. E. *J. Phys. Chem.* **1986**, *90*, 3097–3103.

(18) Joseph, J.; Jemmis, E. D. *J. Am. Chem. Soc.* **2007**, *129*, 4620–4632.

(19) Roncaratti, L.; Belpassi, L.; Cappelletti, D.; Pirani, F.; Tarantelli, F. *J. Phys. Chem. A* **2009**, *113*, 15223–15232.

(20) Belpassi, L.; Reca, M. L.; Tarantelli, F.; Roncaratti, L. F.; Pirani, F.; Cappelletti, D.; Faure, A.; Scribano, Y. *J. Am. Chem. Soc.* **2010**, *132*, 13046–13058.

(21) Cappelletti, D.; Ronca, E.; Belpassi, L.; Tarantelli, F.; Pirani, F. *Acc. Chem. Res.* **2012**, *45*, 1571–1580.

(22) Li, H.; Gordon, M. S.; Jensen, J. H. *J. Chem. Phys.* **2006**, *124*, 214108.

(23) Gresh, N.; Cisneros, G. A.; Darden, T. A.; Piquemal, J.-P. *J. Chem. Theory Comput.* **2007**, *3*, 1960–1986.

(24) Lee, A. J.; Rick, S. W. *J. Chem. Phys.* **2011**, *134*, 184507.

(25) Khoury, L.; Naseem-Khan, S.; Kwapien, K.; Hobaika, Z.; Maroun, R.; Piquemal, J.-P.; Gresh, N. *J. Comput. Chem.* **2017**, *121*, 3997–1920.

(26) Deng, S.; Wang, Q.; Ren, P. *J. Comput. Chem.* **2017**, *38*, 2222–2231.

(27) Phipps, M. J.; Fox, T.; Tautermann, C. S.; Skylaris, C.-K. *Chem. Soc. Rev.* **2015**, *44*, 3177–3211.

(28) Reed, A. E.; Weinhold, F. *J. Chem. Phys.* **1983**, *78*, 4066–4073.

(29) Reed, A. E.; Curtiss, L. A.; Weinhold, F. *Chem. Rev.* **1988**, *88*, 899–926.

(30) Glendening, E. D.; Streitwieser, A. *J. Chem. Phys.* **1994**, *100*, 2900–2909.

(31) Glendening, E. D. *J. Am. Chem. Soc.* **1996**, *118*, 2473–2482.

(32) Glendening, E. D. *J. Phys. Chem. A* **2005**, *109*, 11936–11940.

(33) Stone, A. J. *J. Phys. Chem. A* **2017**, *121*, 1531–1534.

(34) Stone, A. J.; Szalewicz, K. *J. Phys. Chem. A* **2018**, *122*, 733–736.

(35) Jeziorski, B.; Moszynski, R.; Szalewicz, K. *Chem. Rev.* **1994**, *94*, 1887–1930.

(36) Szalewicz, K. *WIREs: Comput. Mol. Sci.* **2012**, *2*, 254–272.

(37) Stone, A. J. *Chem. Phys. Lett.* **1993**, *211*, 101–109.

(38) Stone, A. J.; Misquitta, A. J. *Chem. Phys. Lett.* **2009**, *473*, 201–205.

(39) Misquitta, A. J.; Szalewicz, K. *J. Chem. Phys.* **2005**, *122*, 214109.

(40) Kitaura, K.; Morokuma, K. *Int. J. Quantum Chem.* **1976**, *10*, 325–340.

(41) Morokuma, K. *Acc. Chem. Res.* **1977**, *10*, 294–300.

(42) Stevens, W. J.; Fink, W. H. *Chem. Phys. Lett.* **1987**, *139*, 15–22.

(43) Bagus, P. S.; Hermann, K.; Bauschlicher Jr, C. W. *J. Chem. Phys.* **1984**, *80*, 4378–4386.

(44) Khaliullin, R. Z.; Cobar, E. A.; Lochan, R. C.; Bell, A. T.; Head-Gordon, M. *J. Phys. Chem. A* **2007**, *111*, 8753–8765.

(45) Horn, P. R.; Sundstrom, E. J.; Baker, T. A.; Head-Gordon, M. *J. Chem. Phys.* **2013**, *138*, 134119.

(46) Horn, P. R.; Mao, Y.; Head-Gordon, M. *Phys. Chem. Chem. Phys.* **2016**, *18*, 23067–23079.

(47) Mo, Y.; Gao, J.; Peyerimhoff, S. D. *J. Chem. Phys.* **2000**, *112*, 5530–5538.

(48) Mo, Y.; Song, L.; Lin, Y. *J. Phys. Chem. A* **2007**, *111*, 8291–8301.

(49) Mo, Y.; Bao, P.; Gao, J. *Phys. Chem. Chem. Phys.* **2011**, *13*, 6760–6775.

(50) Boys, S. F.; Bernardi, F. *Mol. Phys.* **1970**, *19*, 553–566.

(51) Khaliullin, R. Z.; Bell, A. T.; Head-Gordon, M. *J. Chem. Phys.* **2008**, *128*, 184112.

(52) Cobar, E. A.; Horn, P. R.; Bergman, R. G.; Head-Gordon, M. *Phys. Chem. Chem. Phys.* **2012**, *14*, 15328–15339.

(53) Bell, F.; Ruan, Q. N.; Golan, A.; Horn, P. R.; Ahmed, M.; Leone, S. R.; Head-Gordon, M. *J. Am. Chem. Soc.* **2013**, *135*, 14229–14239.

(54) Wu, Q.; Ayers, P. W.; Zhang, Y. *J. Chem. Phys.* **2009**, *131*, 164112.

(55) Wu, Q.; Van Voorhis, T. *Phys. Rev. A* **2005**, *72*, 024502.

(56) Wu, Q.; Van Voorhis, T. *J. Chem. Theory Comput.* **2006**, *2*, 765–774.

(57) Kaduk, B.; Kowalczyk, T.; Van Voorhis, T. *Chem. Rev.* **2011**, *112*, 321–370.

(58) Becke, A. D. *J. Chem. Phys.* **1988**, *88*, 2547–2553.

(59) Hirshfeld, F. L. *Theor. Chem. Acc.* **1977**, *44*, 129–138.

(60) Řezáč, J.; de la Lande, A. *J. Chem. Theory Comput.* **2015**, *11*, 528–537.

(61) Lao, K. U.; Herbert, J. M. *J. Chem. Theory Comput.* **2016**, *12*, 2569–2582.

(62) Řezáč, J.; de la Lande, A. *Phys. Chem. Chem. Phys.* **2017**, *19*, 791–803.

(63) Ronca, E.; Belpassi, L.; Tarantelli, F. *ChemPhysChem* **2014**, *15*, 2682–2687.

(64) Reed, A. E.; Weinhold, F.; Curtiss, L. A.; Pochatko, D. J. *J. Chem. Phys.* **1986**, *84*, 5687–5705.

(65) Sokalski, W.; Hariharan, P.; Kaufman, J. J. *J. Phys. Chem.* **1983**, *87*, 2803–2810.

(66) Khaliullin, R. Z.; Bell, A. T.; Head-Gordon, M. *Chem.-Eur. J.* **2009**, *15*, 851–855.

(67) Hayes, I.; Stone, A. *Mol. Phys.* **1984**, *53*, 83–105.

(68) Mao, Y.; Horn, P. R.; Head-Gordon, M. *Phys. Chem. Chem. Phys.* **2017**, *19*, 5944–5958.

(69) Gianinetti, E.; Raimondi, M.; Tornaghi, E. *Int. J. Quantum Chem.* **1996**, *60*, 157–166.

(70) Stoll, H.; Wagenblast, G.; Preuß, H. *Theor. Chem. Acc.* **1980**, *57*, 169–178.

(71) Khaliullin, R. Z.; Head-Gordon, M.; Bell, A. T. *J. Chem. Phys.* **2006**, *124*, 204105.

(72) Azar, R. J.; Horn, P. R.; Sundstrom, E. J.; Head-Gordon, M. *J. Chem. Phys.* **2013**, *138*, 084102.

(73) Horn, P. R.; Head-Gordon, M. *J. Chem. Phys.* **2015**, *143*, 114111.

(74) Wu, Q.; Van Voorhis, T. *J. Phys. Chem. A* **2006**, *110*, 9212–9218.

(75) Wu, Q.; Van Voorhis, T. *J. Chem. Phys.* **2006**, *125*, 164105.

(76) Van Voorhis, T.; Kowalczyk, T.; Kaduk, B.; Wang, L.-P.; Cheng, C.-L.; Wu, Q. *Annu. Rev. Phys. Chem.* **2010**, *61*, 149–170.

(77) Goldey, M. B.; Brawand, N. P.; Vörös, M.; Galli, G. *J. Chem. Theory Comput.* **2017**, *13*, 2581V2590.

(78) Wu, Q.; Yang, W. *J. Chem. Phys.* **2003**, *118*, 2498–2509.

(79) Horn, P. R.; Head-Gordon, M. *J. Chem. Phys.* **2016**, *144*, 084118.

(80) Mo, Y. *J. Chem. Phys.* **2003**, *119*, 1300–1306.

(81) Mo, Y.; Wang, C.; Guan, L.; Braïda, B.; Hiberty, P. C.; Wu, W. *Chem.-Eur. J.* **2014**, *20*, 8444–8452.

(82) Wang, C.; Guan, L.; Danovich, D.; Shaik, S.; Mo, Y. *J. Comput. Chem.* **2016**, *37*, 34–45.

(83) Famulari, A.; Gianinetti, E.; Raimondi, M.; Sironi, M. *Int. J. Quantum Chem.* **1998**, *69*, 151–158.

(84) Shao, Y.; Gan, Z.; Epifanovsky, E.; Gilbert, A. T.; Wormit, M.; Kussmann, J.; Lange, A. W.; Behn, A.; Deng, J.; Feng, X.; Ghosh, D.; Goldey, M.; Horn, P. R.; Jacobson, L. D.; Kaliman, I.; Khaliullin, R. Z.; Kuś, T.; Landau, A.; Liu, J.; Proynov, E. I.; Rhee, Y. M.; Richard, R. M.; Rohrdanz, M. A.; Steele, R. P.; Sundstrom, E. J.; Woodcock, H. L.; Zimmerman, P. M.; Zuev, D.; Albrecht, B.; Alguire, E.; Austin, B.; Beran, G. J. O.; Bernard, Y. A.; Berquist, E.; Brandhorst, K.; Bravaya, K. B.; Brown, S. T.; Casanova, D.; Chang, C.-M.; Chen, Y.; Chien, S. H.; Closser, K. D.; Crittenden, D. L.; Diedenhofen, M.; DiStasio, R. A.; Do, H.; Dutoi, A. D.; Edgar, R. G.; Fatehi, S.; Fusti-Molnar, L.; Ghysels, A.; Golubeva-Zadorozhnaya, A.; Gomes, J.; Hanson-Heine, M. W.; Harbach, P. H.; Hauser, A. W.;

Hohenstein, E. G.; Holden, Z. C.; Jagau, T.-C.; Ji, H.; Kaduk, B.; Khistyaev, K.; Kim, J.; Kim, J.; King, R. A.; Klunzinger, P.; Kosenkov, D.; Kowalczyk, T.; Krauter, C. M.; Lao, K. U.; Laurent, A.; Lawler, K. V.; Levchenko, S. V.; Lin, C. Y.; Liu, F.; Livshits, E.; Lochan, R. C.; Luenser, A.; Manohar, P.; Manzer, S. F.; Mao, S.-P.; Mardirossian, N.; Marenich, A. V.; Maurer, S. A.; Mayhall, N. J.; Neuscamman, E.; Oana, C. M.; Olivares-Amaya, R.; ONeill, D. P.; Parkhill, J. A.; Perrine, T. M.; Peverati, R.; Prociuk, A.; Rehn, D. R.; Rosta, E.; Russ, N. J.; Sharada, S. M.; Sharma, S.; Small, D. W.; Sodt, A.; Stein, T.; Stück, D.; Su, Y.-C.; Thom, A. J.; Tsuchimochi, T.; Vanovschi, V.; Vogt, L.; Vydrov, O.; Wang, T.; Watson, M. A.; Wenzel, J.; White, A.; Williams, C. F.; Yang, J.; Yeganeh, S.; Yost, S. R.; You, Z.-Q.; Zhang, I. Y.; Zhang, X.; Zhao, Y.; Brooks, B. R.; Chan, G. K.; Chipman, D. M.; Cramer, C. J.; Goddard, W. A.; Gordon, M. S.; Hehre, W. J.; Klamt, A.; Schaefer, H. F.; Schmidt, M. W.; Sherrill, C. D.; Truhlar, D. G.; Warshel, A.; Xu, X.; Aspuru-Guzik, A.; Baer, R.; Bell, A. T.; Besley, N. A.; Chai, J.-D.; Dreuw, A.; Dunietz, B. D.; Furlani, T. R.; Gwaltney, S. R.; Hsu, C.-P.; Jung, Y.; Kong, J.; Lambrecht, D. S.; Liang, W.; Ochsenfeld, C.; Rassolov, V. A.; Slipchenko, L. V.; Subotnik, J. E.; Van Voorhis, T.; Herbert, J. M.; Krylov, A. I.; Gill, P. M.; Head-Gordon, M. *Mol. Phys.* **2015**, *113*, 184–215.

(85) Mardirossian, N.; Head-Gordon, M. *Phys. Chem. Chem. Phys.* **2014**, *16*, 9904–9924.

(86) Vydrov, O. A.; Van Voorhis, T. *J. Chem. Phys.* **2010**, *133*, 244103.

(87) Mardirossian, N.; Head-Gordon, M. *Mol. Phys.* **2017**, *115*, 2315–2372.

(88) Burns, L. A.; Faver, J. C.; Zheng, Z.; Marshall, M. S.; Smith, D. G.; Vanommeslaeghe, K.; MacKerell Jr, A. D.; Merz Jr, K. M.; Sherrill, C. D. *J. Chem. Phys.* **2017**, *147*, 161727.

(89) Goerigk, L.; Hansen, A.; Bauer, C. A.; Ehrlich, S.; Najibi, A.; Grimme, S. *Phys. Chem. Chem. Phys.* **2017**,

(90) Mao, Y.; Demerdash, O.; Head-Gordon, M.; Head-Gordon, T. *J. Chem. Theory Comput.* **2016**, *12*, 5422–5437.

(91) Mao, Y.; Shao, Y.; Dziedzic, J.; Skylaris, C.-K.; Head-Gordon, T.; Head-Gordon, M. *J. Chem. Theory Comput.* **2017**, *13*, 1963–1979.

(92) Gill, P. M.; Johnson, B. G.; Pople, J. A. *Chem. Phys. Lett.* **1993**, *209*, 506–512.

(93) Rappoport, D.; Furche, F. *J. Chem. Phys.* **2010**, *133*, 134105.

(94) Weigend, F.; Ahlrichs, R. *Phys. Chem. Chem. Phys.* **2005**, *7*, 3297–3305.

(95) Bauschlicher Jr, C. W.; Bagus, P. S.; Nelin, C. J.; Roos, B. O. *J. Chem. Phys.* **1986**, *85*, 354–364.

(96) Lupinetti, A. J.; Fau, S.; Frenking, G.; Strauss, S. H. *J. Phys. Chem. A* **1997**, *101*, 9551–9559.

(97) Lupinetti, A. J.; Frenking, G.; Strauss, S. H. *Angew. Chem. Int. Ed.* **1998**, *37*, 2113–2116.

(98) Becke, A. D. *J. Chem. Phys.* **1993**, *98*, 5648–5652.

(99) Grimme, S.; Ehrlich, S.; Goerigk, L. *J. Comput. Chem.* **2011**, *32*, 1456–1465.

(100) Hobza, P.; Havlas, Z. *Chem. Rev.* **2000**, *100*, 4253–4264.

(101) Hermansson, K. *J. Phys. Chem. A* **2002**, *106*, 4695–4702.

(102) Demerdash, O.; Mao, Y.; Liu, T.; Head-Gordon, M.; Head-Gordon, T. *J. Chem. Phys.* **2017**, *147*, 161721.

(103) Jiao, D.; King, C.; Grossfield, A.; Darden, T. A.; Ren, P. *J. Phys. Chem. B* **2006**, *110*, 18553–18559.

(104) Piquemal, J.-P.; Perera, L.; Cisneros, G. A.; Ren, P.; Pedersen, L. G.; Darden, T. A. *J. Chem. Phys.* **2006**, *125*, 054511.

(105) Jing, Z.; Qi, R.; Liu, C.; Ren, P. *J. Chem. Phys.* **2017**, *147*, 161733.

(106) Lin, Y.-S.; Li, G.-D.; Mao, S.-P.; Chai, J.-D. *J. Chem. Theory Comput.* **2012**, *9*, 263–272.

(107) Mayer, I.; Salvador, P. *Chem. Phys. Lett.* **2004**, *383*, 368–375.

(108) Matito, E.; Solà, M.; Salvador, P.; Duran, M. *Faraday Discuss.* **2007**, *135*, 325–345.

(109) Salvador, P.; Ramos-Cordoba, E. Communication: An approximation to Bader's topological atom. 2013.

(110) Tafipolsky, M. *J. Phys. Chem. A* **2016**, *120*, 4550–4559.

(111) Misquitta, A. J.; Stone, A. J. *J. Chem. Theory Comput.* **2016**, *12*, 4184–4208.

(112) Legon, A. C. *Phys. Chem. Chem. Phys.* **2010**, *12*, 7736–7747.

(113) Pople, J. A.; Gill, P. M.; Johnson, B. G. *Chem. Phys. Lett.* **1992**, *199*, 557–560.

(114) Handy, N. C.; Schaefer III, H. F. *J. Chem. Phys.* **1984**, *81*, 5031–5033.

(115) Kaduk, B.; Tsuchimochi, T.; Van Voorhis, T. *J. Chem. Phys.* **2014**, *140*, 18A503.

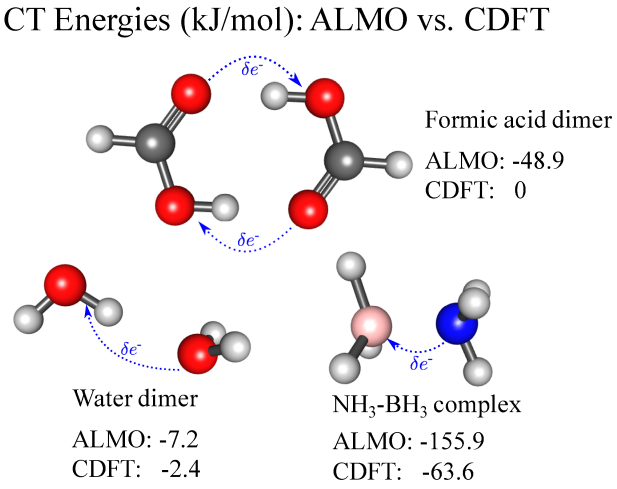

Figure 10: For Table of Contents (TOC) only